The microRNAs miR-302b and miR-372 regulate mitochondrial metabolism via the SLC25A12 transporter, which controls MAVS-mediated antiviral innate immunity

安川, 開

https://doi.org/10.15017/4060013

出版情報：Kyushu University, 2019, 博士（理学）, 課程博士
バージョン：
権利関係：

The microRNAs miR-302b and miR-372 regulate mitochondrial metabolism via the SLC25A12 transporter, which controls MAVS-mediated antiviral innate immunity

Kai Yasukawa

Graduate School of Systems Life Sciences, Kyushu University

GENERAL INTRODUCTION

Mitochondria are essential organelles that produce ATP and are involved in cellular homeostasis maintaining processes, such as apoptosis (1), buffering calcium (2) and aging (3). Mitochondria are encased by a lipid-bilayer that forms unique finger-like structures and are the only organelle outside of the nucleus that maintains part of their own DNA (mtDNA). Moreover, mitochondrial inner membrane forms cristae required for oxidative phosphorylation in the mitochondria. Over ten years ago, the seminal study by Seth et al. demonstrated that mitochondria are involved in antiviral innate immunity (4).

Innate immunity is a ubiquitous system that widely protects organisms from infectious pathogens by functioning as a front-line host defense mechanism. The immune response is triggered by the recognition of broadly conserved microbial components, known as pathogen-associated molecular patterns, by germline-encoded pattern recognition receptors (PRRs) in host cells (5). Functioning as a host defense system against RNA viruses in mammals, the innate immune response is strictly controlled by two distinct pathways mediated by the PRRs (e.g., Toll-like receptor 3; TLR-3 and the retinoic acid-inducible gene I (RIG-I)-like receptors; RLRs), and both the receptors respond to virus-derived RNAs (5, 6). The first pathway is triggered by endosomal expressing TLR-3, which recognizes virus-derived dsRNA that enters the host cell via endocytosis. The second pathway is prompted by either of the two RLRs, RIG-I and/or melanoma differentiation-associated gene 5 (MDA-5), both of which detect cytoplasmic viral dsRNA (7-9). Although the two pathways differ with respect to the initial activation of their downstream effectors, they converge at the point of activation of the transcriptional factors interferon regulatory factor 3 (IRF-3) and nuclear factor κB (NF-κB); this results in the rapid production of type I interferons (IFN-α and -β) and other proinflammatory cytokines for establishing adaptive antiviral immunity (6, 10). In addition, danger-associated molecular

patterns (DAMPs), which are endogenous molecules such as chromatin-associated protein high-mobility group box 1 (HMGB1), heat shock proteins (HSPs), ATP, and uric acid released from damaged or dying cells, trigger sterile inflammation (11). Sterile inflammation is also induced by several PRRs, including TLRs and nucleotide-binding domain leucine-rich repeat-containing receptors (NLRs) such as NLRP3, which recognizes DAMPs and lead to the production of proinflammatory cytokines. Unresolved sterile inflammation is involved in development and progression of diseases such as neurodegenerative diseases and atherosclerosis (11).

Mitochondria act as a platform for innate immune signaling against viral infection or sterile inflammation triggered by some DAMPs (12). Mitochondrial-mediated antiviral immunity depends on the activation of the RLR signaling pathway, and mitochondrial antiviral signaling (MAVS), a downstream adaptor of RLR at the mitochondrial outer membrane; RLR plays a central role in the signal transduction (4, 9). Mitochondrial-mediated antiviral immunity via MAVS is regulated by the host factors and conditions in the mitochondria. When viruses infect cells, MAVS recruits various types of effectors at the mitochondrial outer membrane and forms a MAVS signalosome—a signal-transduction complex. A plethora factors regulate in MAVS-mediated antiviral responses at the mitochondrial outer membrane, including cytosolic and mitochondrial proteins (13).

In addition to these findings, our recent research reveals that MAVS-mediated antiviral responses also depend on the mitochondrial inner membrane conditions. Mitochondrial fusion-defective cells or cells treated with a protonophore CCCP exhibite widespread loss of mitochondrial membrane potential ($\Delta\psi_m$), and the cells with abnormal $\Delta\psi_m$ have defective antiviral innate immune responses (14). The physiological relevance of $\Delta\psi_m$ and innate immune response has been observed in influenza A virus infection. Translocation of influenza A virus protein PB1-F2 into mitochondria leads to $\Delta\psi_m$ attenuation upon viral infection and impairs

cellular antiviral responses (15). These findings indicated that $\Delta\psi_m$ is essential for the activation of MAVS-mediated antiviral responses. On the mitochondrial inner membrane, the electron transport chain produces the ATP to supply energy to the cell. A series of oxidative phosphorylation reactions (OXPHOS) by the electron transport chain is also important for inducing MAVS-mediated antiviral responses and OXPHOS defects, such as lacking mtDNA, diminish antiviral responses (16).

Recently, our study has revealed that mitochondrial inter membrane space also regulates MAVS-mediated antiviral responses. Prohibitin (PHB) complexes are involved in mitochondrial morphology and MAVS-mediated antiviral responses via CLPB1 in the inter membrane space (17). PHBs are ubiquitously expressed mitochondrial inner membrane proteins that form ring-like PHB complexes comprising multiple PHB1 and PHB2 subunits (18) to maintain the inner membrane cristae structure and mitochondrial integrity (19, 20).

Regulation of MAVS-mediated antiviral responses is also controlled post-transcriptionally by microRNAs (miRNAs) that are one of the candidate post-transcriptional regulators. miRNAs are short non-coding RNAs that suppress of multiple genes and are associated with various biological functions, such as cell proliferation, differentiation, development, and apoptosis (21, 22). miRNAs either block protein translation from mRNA or degrade mRNA reducing its stability following an imperfect binding with the 3'-untranslated regions (3'UTR) of target mRNAs via their seed sequence (22-24). So far, more than 2,000 miRNAs have been identified in the human genome, many of which are implicated in human diseases and are expected to be new therapeutic targets (25). Recent studies have revealed that many miRNAs also contribute to antiviral innate immunity (26). Moreover, some miRNAs have been reported to be involved in RLR-mediated antiviral innate immunity by regulating the expression of RLRs and downstream transcriptional factors (26, 27). In macrophages, miR-

146a expression is upregulated by vesicular stomatitis virus (VSV) infection (27, 28). miR-146a negatively regulates VSV-triggered type I IFN production; therefore, promoting VSV replication in macrophages. Inhibition of VSV-triggered type I IFN production occurs via direct suppression of TRAF6, IRAK1, and IRAK2; all of which are downstream signaling molecules of RLR-mediated antiviral innate immunity (28). In the current study has revealed that the expression of some miRNAs is also induced by viral infection and that both miR-302b and miR-372 influence mitochondrial-mediated antiviral innate immunity by regulating mitochondrial dynamics and metabolic demand (29).

Finally, mitochondrial components and function are also associated with NLRP3 inflammasome activity (30). The NLRP3 inflammasome is a complex which is activated upon cellular infection or stress. Inflammasome activation leads to caspase-1-dependent secretion of proinflammatory cytokines such as interleukin-1β (IL-1β) and IL-18 and an inflammatory form of cell death termed as pyroptosis. External NLRP3 activators induce caspase-1- and NLRP3-independent mitochondrial damage and lead to release of mitochondrial components, including mitochondrial reactive oxygen species (mROS), mtDNA, and cardiolipin, all of which promote or directly activate the NLRP3 inflammasome (31-34). In addition to the mitochondrial components, mitochondrial dynamics and membrane potential also influence NLRP3 inflammasome activity (33, 35, 36).

Mitochondria act as a platform for antiviral responses and sterile inflammation. These signal transduction pathways are regulated not only by physical interaction between MAVS signalosome or NLRP3 inflammasome and some regulators but also by indirect interactions separate from those at the mitochondrial outer membrane.

References

1. Wang, X. (2001) The expanding role of mitochondria in apoptosis. *Genes Dev*. **15**, 2922-2933
2. Rutter, G. A. and Rizzuto, R. (2000) Regulation of mitochondria metabolism by ER Ca^{2+} release: an intimate connection. *Trends Biochem. Sci.* **25**, 215-221
3. Raha, S. and Robinson, B. H. (2000) Mitochondria, oxygen free radicals, disease and aging. *Trends Biochem. Sci.* **25**, 502-508
4. Seth, R. B., Sun, L., Ea, C.K., and Chen, Z. J. (2005) Identification and characterization of MAVS, a mitochondrial antiviral signalling protein that activates NF-κB and IRF3. *Cell* **122**, 669-682
5. Kawai, T., and Akira, S. (2006) Innate immune recognition of viral infection. *Nat. Immunol.* **7**, 131-137
6. Meylan, E., and Tschopp, J. (2006) Toll-like receptors and RNA helicases: two parallel ways to trigger antiviral responses. *Mol. Cell* **22**, 561-569
7. Yoneyama, M., Kikuchi, M., Natsukawa, T., Shinobu, N., Imaizumi, T., Miyagishi, M., Taira, K., Akira, S., and Fujita, T. (2004) The RNA helicase RIG-I has an essential function in double-stranded RNA-induced innate antiviral responses. *Nat. Immunol.* **5**, 730-737
8. Kato, H., Takeuchi, O., Sato, S., Yoneyama, M., Yamamoto, M., Matsui, K., Uematsu, S., Jung, A., Kawai, T., Ishii, K.J., Yamaguchi, O., Otsu, K., Tsujimura, T., Koh, C.S., Reis e Sousa, C., Matsuura, Y., Fujita, T., and Akira, S. (2006) Differential roles of MDA5 and RIG-I helicases in the recognition of RNA viruses. *Nature* **441**, 101-105
9. Loo, Y.M., and Gale, M., Jr. (2011) Immune signaling by RIG-I-like receptors. *Immunity* **34**, 680-692
10. Le Bon, A., and Tough, D. F. (2002) Links between innate and adaptive immunity via type I interferon. *Curr. Opin. Immunol.* **14**, 432-436

11. Chen, G. Y., and Nuñez, G. (2010) Sterile inflammation: sensing and reacting to damage. *Nat. Rev. Immunol.* **10**, 826-837
12. Mills, E. L., Kelly, B., and O'Neill, L. A. J. (2017) Mitochondria are the powerhouses of immunity. *Nat. Immunol.* **18**, 488-498
13. Koshiba, T. (2013) Mitochondrial-mediated antiviral immunity. *Biochim. Biophys. Acta.* **1833**, 225-232
14. Koshiba, T., Yasukawa, K., Yanagi, Y., and Kawabata, S. (2011) Mitochondrial membrane potential is required for MAVS-mediated antiviral signaling. *Sci. Signal.* **4**, ra7
15. Yoshizumi, T., Ichinohe, T., Sasaki, O., Otera, H., Kawabata, S., Mihara, K., and Koshiba, T. (2014) Influenza A virus protein PB1-F2 translocates into mitochondria via Tom40 channels and impairs innate immunity. *Nat. Commun.* **5**, 4713
16. Yoshizumi, T., Imamura, H., Taku, T., Kuroki, T., Kawaguchi, A., Ishikawa, K., Nakada, K., and Koshiba, T. (2017) RLR-mediated antiviral innate immunity requires oxidative phosphorylation activity. *Sci. Rep.* **7**, 5379
17. Yoshinaka, T., Kosako, H., Yoshizumi, T., Furukawa, R., Hirano, Y., Kuge, O., Tamada, T., and Koshiba, T. (2019) Structural basis of mitochondrial scaffolds by prohibitin complexes: Insight into a role of the coiled-coil region. *iScience* **19**, 1065-1078
18. Tatsuta, T., Model, K., and Langer, T. (2005) Formation of membrane-bound ring complexes by prohibitins in mitochondria. *Mol. Biol. Cell* **16**, 248-259
19. Artal-Sanz, M., and Tavernarakis, N. (2009) Prohibitin and mitochondrial biology. *Trends Endocrinol. Metab.* **20**, 394-401
20. Osman, C., Haag, M., Potting, C., Rodenfels, J., Dip, P.V., Wieland, F.T., Brügger, B., Westermann, B., and Langer, T. (2009) The genetic interactome of prohibitins: coordinated control of cardiolipin and phosphatidylethanolamine by conserved regulators in mitochondria.

J. Cell Biol. **184**, 583-596

21. Ambros, V. (2004) The functions of animal microRNAs. *Nature* **431**, 350-355
22. Wienholds, E., and Plasterk, R. H. A. (2005) MicroRNA function in animal development. *FEBS Lett.* **579**, 5911-5922
23. Eulalio, A., Huntzinger, E., Nishihara, T., Rehwinkel, J., Fauser, M., and Izaurralde, E. (2009) Deadenylation is a widespread effect of miRNA regulation. *RNA* **15**, 21-32
24. Guo, H., Ingolia, N. T., Weissman J. S., and Bartel, D. P. (2010) Mammalian microRNAs predominantly act to decrease target mRNA levels. *Nature* **466**, 835-840
25. Mendell, J. T., and Olson, E. N. (2012) MicroRNAs in stress signaling and human disease. *Cell* **148**, 1172-1187
26. Nejad, C., Stunden, H. J., and Gantier, M. P. (2018) A guide to miRNAs in inflammation and innate immune responses. *FEBS J.* **285**, 3695-3716
27. Chan, Y. K., and Gack, M. U. (2015) RIG-I-like receptor regulation in virus infection and immunity. *Curr. Opin. Virol.* **12**, 7-14
28. Hou, J., Wang, P., Lin, L., Liu, X., Ma, F., An, H., Wang, Z., and Cao, X. (2009) MicroRNA-146a Feedback Inhibits RIG-I-Dependent Type I IFN Production in Macrophages by Targeting TRAF6, IRAK1, and IRAK2. *J. Immunol.* **183**, 2150-2158
29. Yasukawa, K., Kinoshita, D., Yaku, K., Nakagawa, T., and Koshiba, T. (2020) The microRNAs miR-302b and miR-372 regulate mitochondrial metabolism via the SLC25A12 transporter, which controls MAVS-mediated antiviral innate immunity. *J. Biol. Chem.* **295**, 444-457
30. Liu, Q., Zhanga, D., Hua, D., Zhoub, X., and Zhou, Y. (2018) The role of mitochondria in NLRP3 inflammasome activation. *Mol. Immunol.* **103**, 115-124
31. Elliott, E. I., and Sutterwala, F. S. (2015) Initiation and perpetuation of NLRP3 inflammasome

activation and assembly. *Immunol. Rev.* **265**, 35-52

32. Shimada, K., Crother, T. R., Karlin, J., Dagvadorj, J., Chiba, N., Chen, S., Ramanujan, V. K., Wolf, A. J., Vergnes, L., Ojcius, D. M., Rentsendorj, A., Vargas, M., Guerrero, C., Wang, Y., Fitzgerald, K. A., Underhill, D. M., Town, T., and Arditi, M. (2012) Oxidized mitochondrial DNA activates the NLRP3 inflammasome during apoptosis. *Immunity* **36**, 401-414
33. Zhou, R., Yazdi, A. S., Menu, P., and Tschopp, J. (2011) A role for mitochondria in NLRP3 inflammasome activation. *Nature* **469**, 221-225
34. Iyer, S. S., He, Q., Janczy, J. R., Elliott, E. I., Zhong, Z., Olivier, A. K., Sadler, J. J., Knepper-Adrian, V., Han, R., Qiao, L., Eisenbarth, S. C., Nauseef, W. M., Cassel, S. L., and Sutterwala, F. S. (2013) Mitochondrial cardiolipin is required for Nlrp3 inflammasome activation. *Immunity* **39**, 311-323
35. Ichinohe, T., Yamazaki, T., Koshiba, T., and Yanagi, Y. (2013) Mitochondrial protein mitofusin 2 is required for NLRP3 inflammasome activation after RNA virus infection. *Proc. Natl. Acad. Sci. U. S. A.* **110**, 17963-17968
36. Park, S., Won, J. H., Hwang, I., Hong, S., Lee, H. K., and Yu, J. W. (2015) Defective mitochondrial fission augments NLRP3 inflammasome activation. *Sci. Rep.* **5**, 15489

Contents

ABSTRACT

MicroRNAs (miRNAs) are small non-coding RNAs that suppress the expression of multiple genes and are involved in numerous biological functions and disorders, including human diseases. Here, we report that two miRNAs, miR-302b and miR-372, target mitochondrial-mediated antiviral innate immunity by regulating mitochondrial dynamics and metabolic demand. Using human cell lines transfected with the synthetic analog of viral dsRNA, poly(I:C), or challenged with Sendai virus, we found that both miRNAs are up-regulated in the cells late after viral infection and ultimately terminate the production of type I interferons and inflammatory cytokines. We found that miR-302b and miR-372 are involved in dynamin-related protein 1 (DRP1)-dependent mitochondrial fragmentation and disrupt mitochondrial metabolism by attenuating solute carrier family 25 member 12 (SLC25A12), a member of the SLC25 family. Neutralizing the effects of the two miRNAs through specific inhibitors re-established the mitochondrial dynamics and the antiviral responses. We found that SLC25A12 contributes to regulating the antiviral response by inducing mitochondrial-related metabolite changes in the organelle. Structure-function analysis indicated that SLC25A12, as part of a prohibitin complex, associates with mitochondrial antiviral signaling protein (MAVS) in mitochondria, providing structural insight into the regulation of the mitochondrial-mediated antiviral response. Our results contribute to the understanding of how miRNAs modulate the innate immune response by altering mitochondrial dynamics and metabolic demand. Manipulating the activities of miR-302b and miR-372 may be a potential therapeutic approach to target RNA viruses.

Introduction

MicroRNAs (miRNAs) are short non-coding RNAs (~22 nucleotides) that act to suppress multiple genes widely expressed in eukaryotes, and are linked to numerous biologic functions such as cell proliferation, differentiation, development, and apoptosis (1, 2). A primary mechanistic action of miRNA is that it interferes with mRNA, followed by imperfect annealing with each 3'-UTR of the target genes via their seed sequences that acts to repress translation and/or degradation results in gene silencing (1). To date, more than a thousand miRNAs have been identified in the human genome, many of which are implicated in human diseases (3). Recent studies revealed that several miRNAs also contribute to antiviral innate immunity (4, 5, 6).

In mammals, innate immunity against viral infection requires the activation of multiple signaling steps that culminate in the rapid production of type I interferons (IFN-α and -β) and other proinflammatory cytokines, such as tumor necrosis factor alpha (TNF-α) and regulated on activation normal T-cell expressed and secreted (RANTES, also known as CCL5), that provide first-line host defense. The immune response is triggered by the recognition of broadly conserved viral components, known as pathogen-associated molecular patterns (e.g., dsRNA or 5'-triphosphated single-stranded RNA (5'-pppRNA)) by host-encoded pattern recognition receptors (PRRs), and Toll-like receptor 3 (TLR-3) and retinoic acid-inducible gene I (RIG-I)-like receptors (RLRs) act as the PRRs (7, 8). Especially in the RLR-mediated signal transduction pathway, the mitochondrion – the central powerhouse of eukaryotes – provides a molecular platform for facilitating the signaling event through mitochondrial antiviral signaling protein (MAVS), a downstream adaptor of RLRs located at the mitochondrial outer membrane (MOM) (9, 10). Although MAVS has a key role in signal transduction by recruiting various types of effectors at the MOM to orchestrate the “MAVS signalosome”, our previous studies

demonstrated that fundamental functions of the mitochondria, including the mitochondrial membrane potential (11, 12), activity of oxidative phosphorylation (13), and mitochondrial dynamics (11, 14), are involved in mitochondrial (MAVS)-mediated innate immunity.

In the present study, we investigated the mechanistic and functional roles of miRNAs in mitochondrial-mediated innate immunity. Although some miRNAs were previously demonstrated to be involved in antiviral innate immunity (4, 5, 6, 15), how those miRNAs function to facilitate innate immunity by changing the mitochondrial potentials has remained unclear. We clarified that two miRNAs, miR-302b and miR-372, which are involved in the embryonic stem cell-specific cell cycle and cell reprogramming (16, 17), target mitochondrial-mediated antiviral innate immunity through their regulation of mitochondrial dynamics and metabolic demand. These insights contribute to elucidate the mechanistic roles of the miRNAs essential for mitochondrial-mediated innate immunity, and manipulating these activities may be a potential therapeutic antiviral target.

Results

Searching for microRNAs linked to antiviral innate immunity and mitochondrial dynamics

To elucidate the expression profile of miRNAs in cells that respond to a viral infection event, we first evaluated changes in miRNA expression in human embryonic kidney 293 (HEK293) cells, a widely used human cell line that responds to a synthetic analogue of viral dsRNA, poly(I:C) transfection. We followed 53 miRNAs that were upregulated more than 3-fold in poly(I:C)-transfected cells relative to those in the mock state (Table S1). To confirm that we would be observing a specific response to activation of the RLR-dependent signaling pathway, we induced another viral infection using Sendai virus (SeV), a negative-stranded RNA virus of the *Paramyxoviridae* family. Remarkably, nine miRNA candidates (miR-1250, miR-143, miR-302b, miR-338, miR-372, miR-410, miR-485, miR-520f, and miR-922) were well-matched between these two different stimuli (Fig. 1A and Table S1).

We therefore evaluated whether these miRNAs with increased levels had a role in the RLR signaling pathway. Although the delivery of poly(I:C) into HEK293 cells potently activated an IFN-β luciferase–based reporter (Fig. 1B; NC), co-transfection of each miRNA mimic with poly(I:C) had various effects on the activation of its reporter. Among the nine candidates mentioned above, we confirmed that the delivery of three miRNA mimics (miR-302b, miR-372, and miR-520f) with poly(I:C) was sufficient to inhibit signal transduction (Fig. 1B). Interestingly, the delivery of two miRNA mimics, miR-302b and miR-372, in HeLa cells (widely used for mitochondrial imaging) led to extensively fragmented mitochondria (Fig. 1C and Table 1). These findings suggest that miR-302b and miR-372 affected the activity of both the RLR pathway and mitochondrial morphology. Because miR-302b and miR-372 have homologous seed sequences that can target overlapping genes (18) (TargetScan: http://www.targetscan.org/vert_72/), we mainly analyzed the function of miR-302b and

confirmed the results against miR-372 in the following experiments.

miR-302b acts as a negative regulator of the mitochondrial-mediated antiviral response

Having identified that miR-302b (also miR-372) might link antiviral cellular innate immunity with mitochondrial potentials, we evaluated the functional role of the miRNA involved in mitochondrial-mediated antiviral innate immunity. The kinetic profile of *IFN-β* expression in A549 cells (widely used in viral research) infected with SeV peaked at 6 h post-infection (p.i.) as detected by quantitative PCR (qPCR), and the *IFN-β* mRNA level was sharply decreased at 12 h p.i. (Fig. 1D, *top*), which is a typical antiviral immune response (19). Expression of miR-302b, which was delayed relative to that of *IFN-β*, was induced 12 h after infection and increased for up to 36 h p.i.; this lagging trend in the expression was also observed in cells transfected with poly(I:C) (Fig. 1D, *bottom*; see also Fig. 2A). To verify that the observed RLR-mediated upregulation of miR-302b was not due to a specific characteristic of the cell type we used, we performed the same miRNA induction experiments in other human cell lines, MRC-5 (fetal lung fibroblasts) and HAP-1 (widely used for biomedical and genetic research), and confirmed that both cell types also exhibited increased expression of miR-302b (Fig. 1E and Fig. 2B).

Because altering the level of miR-302b in cells would be consistent with an antiviral immune response (Fig. 1B, D), we hypothesized that the miRNA acts as a modulator of the RLR signaling pathway. To test this hypothesis, we treated HEK293 cells with the miR-302b mimic and assessed their immune response against either viral infection or poly(I:C)-stimulation. The viral-triggered induction of *IFN-β* and other pro-inflammatory cytokines such as *RANTES* or *TNF-α* was dramatically suppressed in cells transfected with the miR-302b mimic (Fig. 1F and Fig. 2C, D). In addition, we confirmed that an abundant presence of the miR-302b mimic in the cells similarly attenuated the phosphorylation of endogenous interferon regulatory factor 3 (IRF-

3; Fig. 1G), a hallmark of IRF-3 activation, and the production of endogenous IFN-β protein (Fig. 1H and Fig. 2E, F). Treatment of HEK293 cells with the miR-302b mimic similarly reduced the activation of both IFN-β and NF-κB reporters in response to overexpression of either the N-terminal CARD domain of RIG-I (designated as RIG-I$^{1-250}$) or MAVS, the MOM protein that acts downstream of RIG-I (Fig. 2G) (9). Most importantly, interfering with either endogenous miR-302b or miR-372 by applying its specific inhibitors to poly(I:C)-stimulated HEK293 (Fig. 3A) or HAP-1 (Fig. 3B) cells sufficiently increased the production of IFN-β. Taken together, these observations indicated that miR-302b (also miR-372) acts as a negative regulator of the mitochondrial-mediated antiviral response and suggests that it would act in the late stage of viral infection.

miR-302b regulates the DRP1-dependent pathway in the mitochondrial fission process

Because the accumulation of miR-302b in HeLa cells leads to remarkable mitochondrial fragmentation that is restored by the presence of its specific inhibitors (Fig. 4A, B and Fig. 5A, B), we next attempted to elucidate whether certain molecules involved in mitochondrial dynamics are associated with the phenomenon. To reveal its mechanistic actions, we performed microarray analysis in HEK293 cells transfected with the miR-302b mimic. Gene expression profiling of the cells revealed an association of miR-302b with the mitochondrial dynamics (Fig. 4C, *left* heat map), especially the mitochondrial fission process. The observed upregulation of *MID49*, *MID51*, and *MFF*, adaptors for dynamin-related protein 1 (DRP1) (20), and significant downregulation of *Ras-related protein 32* (*RAB32*), all of which participate in mitochondrial fission (21, 22, 23), were further confirmed by gene expression analysis with qPCR in the miR-302b-transfected cells (Fig. 4C, *right* graph).

Indeed, the search for target genes against miR-302b using the program TargetScan

revealed that *RAB32* had a putative binding sequence in the 3'-UTR of the mRNA. To confirm the predicted results experimentally, we constructed a reporter plasmid in which the 3'-UTR region of *RAB32* (110-140) was cloned into a *Renilla* luciferase reporter gene. The results of the reporter assay confirmed that the luciferase activity in HEK293 cells transfected with the miR-302b mimic was greatly attenuated when the WT *RAB32* plasmid was co-transfected, whereas co-transfection with its mismatch-induced mutant plasmid had no effect (Fig. 4D and Fig. 5C). Consistent with these results, delivery of the miR-302b mimic into the cells significantly affected the abundance of endogenous RAB32 at both the mRNA (Fig. 5D, E) and protein (Fig. 4E) levels. In addition, we observed that eliminating RAB32 through the action of miR-302b suppressed the phosphorylation of DRP1 at Ser^{637} (Fig. 4F), a hallmark of DRP1 activation (24), as seen in HEK293 cells treated with siRNA against *RAB32* (Fig. 5F).

On the other hand, HEK293 cells transfected with the miR-302b mimic also exhibited increased expression of the DRP1 adaptors MID49 and MID51, as confirmed by the increase in the amounts of their proteins in the cells (Fig. 4G). DRP1 recruitment in the mitochondrial fraction was sufficiently increased in a miR-302b–dependent manner (Fig. 4H), further indicating that our morphologic phenotype resulted in mitochondrial fragmentation (25). Together, these results highlighted the mechanism by which miR-302b is involved in mitochondrial fission via the DRP1-dependent pathway.

miR-302b also targets a mitochondrial transporter, SLC25A12, which modulates MAVS-mediated signaling

The presence of excess fragmented mitochondria ultimately leads to cellular signaling dysfunction, including the mitochondrial-mediated antiviral response (14). Therefore, we next evaluated whether arresting DRP1 activity in cells treated with a miR-302b mimic (Fig. 5G)

would affect RLR-mediated signal transduction. As reported previously (14), depleting endogenous DRP1 in HEK293 cells through its specific siRNA enhanced the induction of both *IFN-β* and *RANTES* in response to poly(I:C) stimulation relative to that in control siRNA-transfected cells (Fig. 4I). On the other hand, the loss of DRP1 in cells treated with the miR-302b mimic also showed potential induction of immune responses compared with controls, but the recovery was only partial in the cells transfected with a negative control mimic (Fig. 4I, NC/*siDRP1* versus miR-302b/*siDRP1*). These findings suggest that some other factors besides mitochondrial morphology are involved in the RLR pathway, leading us to explore the direct involvement in signal transduction.

Thorough analysis of our microarray data revealed that *SLC25A12*, a member of the solute carrier family, was intensively downregulated in miR-302b-transfected HEK293 cells (Fig. 6A). As expected, *SLC25A12* possessed a miR-302b binding sequence in its 3'-UTR (Fig. 6B and Fig. 7A), whose low abundance of protein was experimentally confirmed in cells transfected with the miRNA mimic (Fig. 6C). Strikingly, the antiviral immune responses detected on the basis of the expression of *IFN-β* and *RANTES* in HEK293 cells stimulated by poly(I:C) were significantly decreased in an *SLC25A12*-depleted condition (Fig. 6D). Knockdown of endogenous SLC25A12 in the cells similarly reduced IFN-β reporter activation in response to the overexpression of either RIG-I$^{1\text{-}250}$ or MAVS constructs (Fig. 7B). We also verified the antiviral immune function of SLC25A12 using *SLC25A12*-deficient HAP-1 cells (Fig. 6E). Because SLC25A12, an aspartate-glutamate transporter localized in the mitochondrial inner membrane (MIM) (26), is required for regulating antiviral signaling through MAVS, it is likely that SLC25A12 acts downstream of MAVS in the pathway.

SLC25A12 associates with MAVS in mitochondria

While exploring the mechanisms of action of SLC25A12, we found that the transporter co-immunoprecipitated with endogenous MAVS in HEK293 cells under physiologic conditions (Fig. 8A). We therefore performed a structure-function analysis to fill the topologic gap between SLC25A12 and MAVS. Using a coimmunoprecipitation approach, we mapped the region of SLC25A12 that interacts with MAVS via the C-terminal region (Fig. 8B) that faces the intermembrane space (IMS) with an unknown function (27). Consistent with the immunoprecipitation results, fluorescence microscopy confirmed the colocalization of both SLC25A12 and MAVS in HeLa cells (Fig. 8C). We explored additional molecules that might bridge SLC25A12 and MAVS at the IMS and found that prohibitins (PHB1 and PHB2), mitochondrial scaffolds localized in the MIM (28), associated with SLC25A12 (Fig. 8A, D). We assume that SLC25A12, as a part of the PHB interactome (28), interacts with MAVS in mitochondria.

Interestingly, decreasing SLC25A12 in cells affected the structural features of MAVS activation accompanied by RLR-mediated signal transduction, *i.e.*, homotypic oligomerization (29, 30) at the MOM (Fig. 8E, F), which further highlights the importance of the transporter in the activation of the signaling pathway. In addition, *SLC25A12*-specific siRNA had no effect on IFN-β reporter activation in response to the overexpression of TANK-binding kinase 1 (TBK-1) (Fig. 7B), a kinase that targets IRF-3, despite the fact that the effector acts downstream of MAVS (9). On the basis of these findings together, we propose a model in which SLC25A12 inhibits the RLR pathway downstream of MAVS (and/or at the same level) and upstream of the kinase TBK-1.

miR-302b regulates mitochondrial metabolism via SLC25A12, which controls antiviral responses

The results described above prompted us to investigate the functional role of SLC25A12 in the regulation of the antiviral response. Because SLC25A12 is a member of the malate-aspartate NADH shuttle (31, 32), we assessed its ability to transfer reducing equivalents. Treatment with the miR-302b mimic significantly decreased the level of NADH in HEK293 cells without changing NAD, resulting in a ~50% greater NAD/NADH ratio (Fig. 9A), which indicated impaired mitochondrial metabolism. Metabolome analysis of the miRNA-transfected cells further revealed that the amounts of aspartate, malate, and pyruvate were similarly decreased in cells treated with the miR-302b mimic, whereas the amount of lactate was increased (Fig. 9B). Consistent with our observations, a decrease in the oxygen consumption rate (OCR) indicated that the miR-302b–targeted mitochondria in the cells became less active (Fig. 9C and Fig. 10A), and the cellular metabolism shifted to glycolytic conditions (Fig. 9D).

We confirmed that the observed regulation of mitochondrial-related metabolites was mainly due to the function of SLC25A12 on the basis of diminishing SLC25A12 in cells with a lower OCR (Fig. 9E and Fig. 10B). To explore whether these metabolic changes in the mitochondria correlated with RLR pathway activation, we performed a signaling assay. As expected, the immunodeficiency observed in the *siSLC25A12*-treated HEK293 cells was significantly recovered by adding aspartate to the media (Fig. 9F), similar to the OCR patterns in *SLC25A12*-deficient cells (Fig. 10C). In addition to the substantial contribution of SLC25A12 to mitochondrial metabolism, we identified that miR-302b targets mitochondrial pyruvate carrier 1 (MPC1) (33, 34) (Fig. 10D, E) and changes in the amount of its protein partially affect mitochondrial respiration (Fig. 10B). Taken together, these findings indicate that the absence of mitochondrial metabolites leads to defective mitochondrial-mediated antiviral signaling.

Discussion

MicroRNAs are known to be involved in various cellular functions, and several miRNAs are triggered by an immune response to induce IFNs (35, 36). Here, we report that two miRNAs, miR-302b and miR-372, potentially attenuate viral-triggered induction of IFN-β and pro-inflammatory cytokines by manipulating mitochondrial functions, such as mitochondrial dynamics and metabolism.

Although much attention has been focused on the identification and characterization of signaling molecules that activate and/or inactivate mitochondrial-mediated antiviral innate immunity, our study explored the mechanistic basis of how these molecules are regulated at the mRNA level and the involvement of the translated products in the signaling event. On the basis of our findings, we propose that miR-302b and miR-372 regulate mitochondrial-mediated antiviral responses by controlling the expression of mitochondrial proteins (such as SLC25A12) to prevent excessive progression of the antiviral response (Fig. 9G). In addition to revealing the mechanistic action of these miRNAs, the findings of the present study may pave the way for understanding an unexpected role of these miRNAs as a therapeutic target for attenuating excess inflammation, such as a cytokine storm because of their high potency for downregulating pro-inflammatory cytokines.

Finally, a previous study revealed that miR-302a, a member of the miR302 family encoded in the human miR302-367 cluster (37), suppresses influenza A virus, an RNA virus of the *Orthomyxoviridae* family, stimulates interferon regulatory factor-5 (IRF-5) expression, and inhibits the production of IFNs and inflammatory cytokines (38). The seed sequences of miR-302b and miR-372 are homologous with that of miR-302a, indicating that both miR-302b and miR-372 would likely act as negative regulators of IRF-5 to prevent the induction of a cytokine storm, as in the case of miR-302a. Therefore, miR-302b and miR-372 may function as potential

regulators of the influenza A virus-induced cytokine storm and provide a candidate target for the treatment of influenza A virus infection.

In our previous studies, we have elucidated that MAVS-mediated antiviral innate immunity is associated with mitochondrial function. These findings demonstrate that activity of MAVS signalosome is regulated not only by direct interaction with MAVS signalosome, but also by indirect interaction with MAVS separate from those at the mitochondrial outer membrane. Our latest study reveals that the PHB complex is involved in mitochondrial morphology and MAVS-mediated antiviral innate immune responses via CLPB1 in the inter membrane space (28). PHBs are ubiquitously expressed mitochondrial inner membrane proteins that form ring-like PHB complexes comprising multiple PHB1 and PHB2 subunits (39) to maintain the cristae structure of the inner membrane and mitochondrial integrity (40, 41). Similarly, SLC25A12 also interacts with PHBs and takes part in PHB complexes to regulate MAVS in the inter membrane space. Intriguingly, SLC25A12 also maintains mitochondrial metabolites such as aspartate, and the absence of mitochondrial metabolites leads to defective mitochondrial-mediated antiviral signaling. Moreover, induction of miR-302b and miR-372 in cells decreases mitochondrial OCR and leads to metabolic shift from the citric-acid cycle to glycolysis followed by increased lactate production. Because lactate acts as the negative regulator of the MAVS-mediated innate immune responses (42), induction of miR-302b and miR-372 also suppress the MAVS-mediated innate immune responses. These results are consistent with the previous findings which demonstrated that the mitochondrial metabolites and mitochondrial metabolic state are involved in innate immune signaling (43, 44).

These recent discoveries strongly suggest that manipulating mitochondrial function can be a new therapeutic approach for treating viral infections and inflammatory diseases. Moreover, miRNAs may also become a drug target.

Materials & Methods

Reagents. Poly(I:C) was purchased from InvivoGen (San Diego, CA), and enzyme-linked immunosorbent assay (ELISA) kits for human IFN-β were supplied by Kamakura Techno-Science Inc (Kanagawa, Japan) and R&D Systems (Minneapolis, MN). All other reagents were biochemical research grade.

Cell lines and viruses. HEK293, HeLa, A549, and MRC-5 cells were maintained in Dulbecco's modified Eagle's medium (GIBCO BRL) supplemented with 1% L-glutamine, penicillin (100 U/mL)-streptomycin (100 μg/mL), and 10% fetal bovine serum at 5% CO_2 and 37° C. The human *SLC25A12* knockout HAP-1 cell line edited by the CRISPR/Cas system was obtained from Horizon Discovery (Cambridge, UK) and maintained in Iscove's Modified Dulbecco's medium (GIBCO BRL) supplemented with 1% GlutaMAX, penicillin (100 U/mL)-streptomycin (100 μg/mL) and 10% fetal bovine serum at 5% CO_2 and 37° C. Sendai virus Cantell strain was purchased from the American Type Culture Collection (Manassas, VA).

Antibodies. Anti-SLC25A12 (ab200201, 1:4000), anti-IRF3 (phosphor Ser386; ab76493, 1:2000), anti-REA/PHB2 (ab181838, 1:5000) rabbit mAbs, anti-MAVS (ab31334, 1:1000) rabbit polyclonal antibody (pAb), and anti-*c*-myc (9E10, 1:1000) mouse mAb were purchased from Abcam (Cambridge, MA). Anti-β-actin (sc-47778, 1:1000) mouse mAb was purchased from Santa Cruz Biotechnology (Dallas, TX). Anti-MID49 (16413-1-AP, 1:1000) and anti-MID51 (20164-1-AP, 1:1000) rabbit pAbs were purchased from Proteintech (Rosemont, IL). Anti-RAB32 (SAB4200086, 1:1000) rabbit pAb and anti-hemagglutinin (HA; HA-7, 1:2000) mAb were purchased from Sigma-Aldrich (St. Louis, MO). Anti-DRP1 (D6C7, 1:1000), anti-DRP1 (phosphor Ser637; D3A4, 1:1000), anti-MPC1 (D2L9I, 1:1000), anti-GAPDH (14C10

Biotinylated, 1:1000), anti-VDAC (D73D12, 1:1000) rabbit mAbs, and anti-PHB1 (Cat #2426, 1:1000) rabbit pAb were supplied from Cell Signaling Technology (Danvers, MA). Anti-mitochondrial heat shock protein 70 (mtHSP70; JG1, 1:1000) mouse mAb, anti-MAVS (PA5-17256, 1:100) rabbit pAb, and the Alexa Fluor 568 (Cat #A11031, 1:400) conjugated goat anti-mouse IgG pAb were purchased from Thermo Fisher Scientific (Waltham, MA). A list of all Abs used in the present study is provided in the Key Resources Table.

Plasmids. The plasmids encoding human MAVS variants and hRIG-I$^{1\text{-}250}$ were described previously (30, 39). To construct reporter plasmids for the SLC25A12, Rab32, and MPC1 target sequence in 3'-UTR, synthetic oligonucleotides encoding 3'-UTR residues containing a 5' *Xho*I restriction site and their anti-sense oligonucleotides containing a 3' *Not*I site were cloned into a psiCHECK-2 plasmid (Promega, Madison, WI). The oligonucleotides used for inserts were as follows: sense, *5′-tcgagagactctgctttgcacagcttgcacttacagc-3′*; antisense, *5′-ggccgctgtaagtgcaagctgtgcaaagcagagtctc-3′* (SLC25A12 3'-UTR); sense, *5′-tcgaggcagcaccact gggcgcctgcacttatttggc-3′*; antisense, *5′-ggccgccaaataagtgcaggcgcccagtggtgctgcc-3′* (RAB32 3'-UTR); and sense, *5′-tcgaggaacaaaatttgtaaccactagcacttaaggc-3′*; antisense, *5′-ggccgccttaagtgc tagtggttacaaattttgttcc- 3′* (MPC1 3'-UTR).

RNA interference and miRNA mimic/inhibitor introduction. For RNA interference and miRNA mimic/inhibitor introduction experiments, siRNAs and miRNA mimics/inhibitors were purchased from Qiagen (GeneSolution siRNA) and Ambion (mirVana miRNA mimics & inhibitors), respectively. For siRNAs, we used *SLC25A12* (SI00054929), *RAB32* (SI00092246), *MPC1* (SI04153415), and *5′-AUUUACCCCAUUCUUCUGCTT-3′* sequence against DRP1. AllStars Negative Control siRNA was used for the negative controls. For miRNA mimics and their

inhibitors, miR-302b mimic (MC10081), miR-302b inhibitor (MH10081), miR-372 mimic (MC10165), and miR-372 inhibitor (MH10165) were used in the study. mirVana miRNA Mimic (Negative Control #1) and mirVana miRNA Inhibitor (Negative Control #1) were used for each negative control, respectively. In the experiments, HEK293 cells were transfected with either 10 nM siRNA or miRNA (final concentration) using Lipofectamine RNAiMAX (Thermo Fisher Scientific) following the manufacturer's protocols. At 48 h after treatment, the cells were used for each functional assay.

Reverse transcription qPCR. Total RNA was isolated from cells with an miRNeasy Mini Kit (Qiagen, Hilden, Germany) or a Maxwell 16 LEV simplyRNA Cell Kit (Promega) according to the manufacturer's protocol, and 500 ng of total RNA was reverse-transcribed with a QuantiTect Reverse Transcription Kit (Qiagen) or TaqMan MicroRNA Reverse Transcription Kit (Thermo Fisher Scientific) to generate cDNAs. Real-time PCR assays were performed with a TaqMan Gene Expression assay using the indicated probes.

ELISA. Production of IFN-β was measured with species-specific ELISA reagents for human IFN-β from Kamakura Techno-Science Inc. and R&D Systems.

Confocal microscopy. Cells were plated on coverslips in 12-well plates (5×10^4 cells/well). The following day, the cells were fixed with 4% paraformaldehyde for 15 min, permeabilized with 0.2% Triton X-100 in 1× PBS (pH 7.2), and blocked with 5% fetal bovine serum. Mitochondria were visualized by using either mitochondrial-targeted red fluorescent protein (12) (Mito-RFP; Fig. 1C) or staining with anti-mtHSP70 (Fig. 3A and Fig. S2A, G) or MAVS (Fig. 5C) pAbs followed by Alexa Fluor 568-conjugated polyclonal and Alexa Fluor 488-conjugated polyclonal

secondary Abs, respectively. Cells were imaged with a C2+ confocal microscope (Nikon Instruments Inc.).

Luciferase reporter assay. HEK293 cells were plated in 96-well plates (3×10^4 cells/well). On the same day, the cells were co-transfected with 40 ng luciferase reporter plasmid (p125luc or pELAM), 4 ng *Renilla* luciferase internal control vector phRL-TK (Promega), and each of the indicated expression plasmids or poly(I:C) (500 ng) using Lipofectamine 2000 reagent (Invitrogen, Carlsbad, CA) following the manufacturer's protocols. The cells were harvested 24 h after transfection and analyzed using a Dual-Glo Luciferase Assay System (Promega). Relative luciferase activity was calculated by normalizing luciferase activity by the *Renilla* luciferase activity expressed in internal control plasmids, and dividing by the normalized value of the control in which only an empty vector (pcDNA3.1) was transfected. Each experiment was replicated at least three independent reproducible results. The p125luc and pELAM reporter plasmids were provided by T. Taniguchi (University of Tokyo, Japan) and T. Seya (Hokkaido University, Japan), respectively.

BRET assay. BRET experiments were performed as described previously (30) with minor modifications. HEK293 cells were transfected with miRNA mimics. At 48 h after the treatment, the miRNA mimic-transfected cells were plated in a 96-well microplate and transfected with 5 ng Nanoluc-tagged MAVS plasmid and increasing amounts of Venus-tagged MAVS constructs using Lipofectamine 2000 at the same time. Twenty hours after transfection, 0.1 μL Nanoluc substrate was added to each well, followed by 1 min of gentle mixing, and luminescence was measured simultaneously for the donor (λ_{em}= 460 nm; short wavelength) and acceptor (λ_{em}= 515 nm; long wavelength).

Immunoprecipitation. Coimmunoprecipitation experiments were performed as described previously (45) with minor modifications. HEK293 cells at 80% confluence were transiently transfected with the appropriate plasmids (1.25 μg each) in a six-well plate using the FuGENE HD transfection reagent (Promega). The following day, the cells were lysed with 1 mL of radioimmunoprecipitation assay (RIPA) buffer with a protease inhibitor cocktail, and the clarified supernatants were incubated overnight at 4° C with anti-c-myc agarose beads (Sigma-Aldrich). After four washes with 1× PBS (pH 7.2), the immunoprecipitates were resolved by 10% SDS-PAGE and analyzed by Western blotting with a mAb against HA followed by a horseradish peroxidase-conjugated antibody against mouse IgG (Cell Signaling Technology). To immunoprecipitate endogenous MAVS, PHB1, or PHB2, HEK293 cells in a 10-cm dish were washed once with 1× PBS (pH 7.2), lysed with 2 mL of RIPA buffer containing protease inhibitor cocktail, and the clarified supernatants were incubated with 10 μg anti-SLC25A12 rabbit mAb followed by incubation overnight at 4° C with 25 μL protein A Sepharose beads. The beads were washed four times with 1× PBS (pH 7.2), and the immunoprecipitates were resolved by 10% SDS-PAGE and immunoblotted with each Ab.

Mitochondrial fractionation. The cells were harvested and washed once with cold 1× PBS (pH 7.2) and resuspended in 700 μL homogenization buffer (20 mM HEPES (pH 7.4), 70 mM sucrose, and 220 mM mannitol) by 30 strokes in a Dounce homogenizer. The homogenate was centrifuged at 800 × *g* for 10 min, and the resulting supernatant was further centrifuged at 10,000 × *g* for 10 min at 4° C to precipitate the crude mitochondrial fraction. The resultant supernatant was centrifuged at 20,000 × *g* for 30 min to obtain the cytosol fraction. The crude mitochondrial fraction was resuspended in homogenization buffer and applied to a discontinuous Percoll

gradient comprising 80%, 52%, and 26% (w/v) Percoll diluted in homogenization buffer. Centrifugation was performed at 43,000 × *g* for 45 min. The purified mitochondrial fraction was recovered from the interface between the 52% and 26% (w/v) Percoll.

Mitochondrial respiration and glycolysis analysis. Mitochondrial respiration and glycolysis analysis were performed using the Seahorse XFe96 Analyzer (Agilent Technologies, Santa Clara, CA). HEK293 cells were seeded on XFe96 Spheroid Microplates (6×10^4 cells/well) the day before the experiment and analyzed using the Seahorse XF Cell Mito Stress Test Kit or the Seahorse XF Glycolysis Stress Test Kit according to the manufacturer's protocols. Before measuring mitochondrial OCR, the culture medium was replaced with XF base medium supplemented with 1 mM pyruvate, 10 mM glucose and 2 mM L-glutamine. First, the baseline values were measured three times, and the mitochondrial OCR in each state was then measured three times after adding the mitochondrial respiratory chain inhibitors to the cells. Oligomycin (2 μM), FCCP (1.5 μM), and rotenone/antimycin A (0.5 μM) were used as mitochondrial respiratory chain inhibitors. The obtained data were analyzed using Wave 2.4.0 software (Agilent Technologies).

Microarray analysis. Total RNA was isolated from cells transfected with the negative control miRNA mimic or miR-302b mimic 72 h later using an miRNeasy Mini Kit (Qiagen) according to the manufacturer's protocol. RNA samples were quantified using an ND-1000 spectrophotometer (NanoDrop Technologies, Wilmington, DE) and the quality was confirmed with an Experion System (Bio-Rad Laboratories, Hercules, CA). The cRNA was amplified, labeled (Low Input Quick Amp Labeling Kit), and hybridized to the SurePrint G3 Human GE v3 8x60K microarray according to the manufacturer's instructions (Agilent Technologies). All

hybridized microarray slides were scanned by an Agilent scanner (Agilent Technologies). Relative hybridization intensities and background hybridization values were calculated using Agilent Feature Extraction Software (ver. 9.5.1.1). Raw signal intensities and flags for each probe were calculated from the hybridization intensities (gProcessedSignal) and spot information (gIsSaturated, etc.) according to the procedures recommended by Agilent. The raw signal intensities of four samples were normalized by a quantile algorithm with the 'preprocessCore' library package (46) of the Bioconductor software (47). To identify upregulated or downregulated genes, we calculated the Z-scores (48) and ratios (non-log scaled fold-change) from the normalized signal intensities of each probe to compare between control and experimental samples, and established criteria for regulated genes: Z-score ≥2.0 and ratio ≥1.5-fold for upregulated genes, and Z-score ≤−2.0 and ratio ≤0.66 for downregulated genes, respectively. The GEO accession number for the microarray data reported in the paper is GSE129615.

Metabolite measurement for LC-MS and gas chromatography GC-MS. Metabolites were extracted from cultured cell pellets using water:methanol:chloroform (1:1:2), and the aqueous phase was preserved. For LC/MS experiments, the dried metabolites were dissolved in 50 μL LC/MS grade water (Wako Pure Chemical Industries, Osaka, Japan) and then filtered with a 0.45-μm Millex filter unit (Merck Millipore, Burlington, MA). For gas chromatography-mass spectrometry experiments, derivatization of the samples was carried out in two steps using methoximation and N-methyl-N-trimethylsilyltrifluoroacetamide with 1% trimethylchlorosilane (MSTFA + 1% TMCS, Pierce) as described previously. Levels of NAD and NADH were determined by multiple reaction monitoring using an Agilent 6460 Triple Quad mass spectrometer coupled with an Agilent 1290 HPLC system. The MS settings and chromatographic conditions used were described previously (49). Tricarboxylic acid cycle intermediates were analyzed by

selected ion monitoring using an Agilent 5977 MSD single Quad mass spectrometer coupled with Agilent 7890 Gas Chromatography as described previously (50). Metabolite amounts were calculated by the integrated sum of the area using Mass Hunter Quantitative software (Agilent Technologies).

Statistical analysis. An analysis of variance test (GraphPad Prism) was used for the statistical analyses. We considered different populations of cells to be biologic replicates; aliquoting or repeated measurements of a cell population was considered to represent technical replicates. We performed at least 3 independent reproducible results for most key experiments, although we did not perform explicit power calculations. Data are presented as the mean ± standard deviation (SD). Statistical significance was assessed by Student's *t*-test. A *P*-value of less than 0.05 was considered statistically significant.

Acknowledgments

First, I would like to express my profound thanks to Dr. Takumi Koshiba (Professor of Fukuoka University) for giving me a chance to study such an interesting subject and for his cordial guidance and encouragement.

I would also like to thank Dr. Shun-ichiro Kawabata (Professor of Kyushu University) for his cordial encouragement and Dr. Takashi Nakagawa and Dr. Keisuke Yaku (Toyama University) for performing metabolome analyses of cell culture and for helpful discussion.

Additionally, I would like to appreciate Daisuke Kinoshita (Kyushu University) for performing the confocal fluorescence microscopy and Yuko Fuchigami (Kyushu University) for her technical assistance with DNA cloning and sequencing.

References

1. Ambros, V. (2004) The functions of animal microRNAs. *Nature* **431**, 350-355
2. Wienholds, E., and Plasterk, R. H. A. (2005) MicroRNA function in animal development. *FEBS Lett.* **579**, 5911-5922
3. Mendell, J. T., and Olson, E. N. (2012) MicroRNAs in stress signaling and human disease. *Cell* **148**, 1172-1187
4. Li, Y., and Shi, X. (2013) MicroRNAs in the regulation of TLR and RIG-I pathways. *Cell. Mol. Immunol.* **10**, 65-71
5. Yarbrough, M.L., Zhang, K., Sakthivel, R., Forst, C.V., Posner, B.A., Barber, G.N., White, M.A., and Fontoura, B. M. A. (2014) Primate-specific miR-576-3p sets host defense signalling threshold. *Nat. Commun.* **5**, 4963
6. Ingle, H., Kumar, S., Raut, A. A., Mishra, A., Kulkarni, D. D., Kameyama, T., Takaoka, A., Akira, S., and Kumar, H. (2015) The microRNA miR-485 targets host and influenza virus transcripts to regulate antiviral immunity and restrict viral replication. *Sci. Signal.* **8**, ra126
7. Kawai, T., and Akira, S. (2006) Innate immune recognition of viral infection. *Nat. Immunol.* **7**, 131-137
8. Meylan, E., and Tschopp, J. (2006) Toll-like receptors and RNA helicases: two parallel ways to trigger antiviral responses. *Mol. Cell* **22**, 561-569
9. Seth, R. B., Sun, L., Ea, C.K., and Chen, Z. J. (2005) Identification and characterization of MAVS, a mitochondrial antiviral signalling protein that activates NF-κB and IRF3. *Cell* **122**, 669-682
10. Koshiba, T. (2013) Mitochondrial-mediated antiviral immunity. *Biochim. Biophys. Acta.* **1833**, 225-232
11. Koshiba, T., Yasukawa, K., Yanagi, Y., and Kawabata, S. (2011) Mitochondrial membrane

potential is required for MAVS-mediated antiviral signaling. *Sci. Signal.* **4**, ra7

12. Yoshizumi, T., Ichinohe, T., Sasaki, O., Otera, H., Kawabata, S., Mihara, K., and Koshiba, T. (2014) Influenza A virus protein PB1-F2 translocates into mitochondria via Tom40 channels and impairs innate immunity. *Nat. Commun.* **5**, 4713.
13. Yoshizumi, T., Imamura, H., Taku, T., Kuroki, T., Kawaguchi, A., Ishikawa, K., Nakada, K., and Koshiba, T. (2017) RLR-mediated antiviral innate immunity requires oxidative phosphorylation activity. *Sci. Rep.* **7**, 5379
14. Castanier, C., Garcin, D., Vazquez, A., and Arnoult, D. (2010) Mitochondrial dynamics regulate the RIG-I-like receptor antiviral pathway. *EMBO Rep.* **11**, 133-138
15. Wan, S., Ashraf, U., Ye, J., Duan, X., Zohaib, A., Wang, W., Chen, Z., Zhu, B., Li, Y., Chen, H., and Cao, S. (2016) MicroRNA-22 negatively regulates poly(I:C)-triggered type I interferon and inflammatory cytokine production via targeting mitochondrial antiviral signaling protein (MAVS). *Oncotarget* **7**, 76667-76683
16. Subramanyam, D., Lamouille, S., Judson, R. L., Liu, J. Y., Bucay, N., Derynck, R., and Blelloch, R. (2011) Multiple targets of miR-302 and miR-372 promote reprogramming of human fibroblasts to induced pluripotent stem cells. *Nat. Biotechnol.* **29**, 443-448
17. Lin, S. L., Chang, D.C., Lin, C.H., Ying, S.Y., Leu, D., and Wu, D.T.S. (2011) Regulation of somatic cell reprogramming through inducible mir-302 expression. *Nucleic Acids Res.* **39**, 1054-1065
18. Agarwal, V., Bell, G. W., Nam, J. W., and Bartel, D. P. (2015) Predicting effective microRNA target sites in mammalian mRNAs. *eLife* **4**, e05005
19. Whittemore, L.A., and Maniatis, T. (1990) Postinduction turnoff of beta-interferon gene expression. *Mol. Cell. Biol.* **10**, 1329-1337
20. Otera, H., Ishihara, N., and Mihara, K. (2013) New insights into the function and regulation

of mitochondrial fission. *Biochim. Biophys. Acta.* **1833**, 1256-1268

21. Alto, N. M., Soderling, J., Scott, J. D. 2002. Rab32 is an A-kinase anchoring protein and participates in mitochondrial dynamics. *J. Cell Biol.* **158**, 659-668
22. Bui, M., Gilady, S. Y., Fitzsimmons, R. E. B., Benson, M. D., Lynes, E. M., Gesson, K., Alto, N. M., Strack, S., Scott, J. D., and Simmen, T. (2010) Rab32 modulates apoptosis onset and mitochondria-associated membrane (MAM) properties. *J. Biol. Chem.* **285**, 31590-31602
23. Cribbs, J.T., and Strack, S. (2007) Reversible phosphorylation of Drp1 by cyclic AMP-dependent protein kinase and calcineurin regulates mitochondrial fission and cell death. *EMBO Rep.* **8**, 939-944
24. Chang, C. R., and Blackstone, C. (2007) Cyclic AMP-dependent protein kinase phosphorylation of Drp1 regulates its GTPase activity and mitochondrial morphology. *J. Biol. Chem.* **282**, 21583–21587
25. Losón, O.C., Song, Z., Chen, H., and Chan, D.C. (2013) Fis1, Mff, MiD49, and MiD51 mediate Drp1 recruitment in mitochondrial fission. *Mol. Biol. Cell* **24**, 659-667
26. Palmieri, L., Pardo, B., Lasorsa, F. M., del Arco, A., Kobayashi, K., Iijima, M., Runswick, M. J., Walker, J. E., Saheki, T., Satrústegui, J., and Palmieri, F. (2001) Citrin and aralar1 are Ca^{2+}-stimulated aspartate/glutamate transporters in mitochondria. *EMBO J.* **20**, 5060-5069
27. Thangaratnarajah, C., Ruprecht, J. J., and Kunji, E. R. S. (2014) Calcium-induced conformational changes of the regulatory domain of human mitochondrial aspartate/glutamate carriers. *Nature Commun.* **5**, 5491
28. Yoshinaka, T., Kosako, H., Yoshizumi, T., Furukawa, R., Hirano, Y., Kuge, O., Tamada, T., and Koshiba, T. (2019) Structural basis of mitochondrial scaffolds by prohibitin complexes: Insight into a role of the coiled-coil region. *iScience* **19**, 1065-1078
29. Hou, F., Sun, L., Zheng, H., Skaug, B., Jiang, Q-X., and Chen, Z. J. (2011) MAVS forms

functional prion-like aggregates to activate and propagate antiviral innate immune response. *Cell* **146**, 448-461

30. Sasaki, O., Yoshizumi, T., Kuboyama, M., Ishihara, T., Suzuki, E., Kawabata, S., and Koshiba, T. (2013) A structural perspective of the MAVS-regulatory mechanism on the mitochondrial outer membrane using bioluminescence resonance energy transfer. *Biochim. Biophys. Acta.* **1833**, 1017-1027
31. Amoedo, N. D., Punzi, D., Obre, E., Lacombe, D., De Grassi, A., Pierri, C. L., and Rossignol, R. (2016) AGC1/2, the mitochondrial aspartate-glutamate carriers. *Biochim. Biophys. Acta.* **1863**, 2394-2412
32. Alkan, H. F., Walter, K. E., Luengo, A., Madreiter-Sokolowski, C. T., Stryeck, S., Lau, A. N., Al-Zoughbi, W., Lewis, C. A., Thomas, C.J., Hoefler, G., Graier, W.F., Madl, T., Vander Heiden, M. G., and Bogner-Strauss, J. G. (2018) Cytosolic aspartate availability determines cell survival when glutamine is limiting. *Cell Metab.* **28**, 1-15
33. Patterson, J. N., Cousteils, K., Lou, J. W., Manning Fox, J. E., MacDonald, P. E., and Joseph, J. W. (2014) Mitochondrial metabolism of pyruvate is essential for regulating glucose-stimulated insulin secretion. *J. Biol. Chem.* **289**, 13335-13346
34. Vakanti, N.M., Divakaruni, A.S., Green, C.R., Parker, S.J., Henry, R.R., Ciaraldi, T.P., Murphy, A.N., Metallo, C. M. (2014) Regulation of substrate utilization by the mitochondrial pyruvate carrier. *Mol. Cell* **56**, 425-435
35. Chan, Y. K., and Gack, M. U. (2015) RIG-I-like receptor regulation in virus infection and immunity. *Curr. Opin. Virol.* **12**, 7-14
36. Forster, S. C., Tate, M. D., and Hertzog, P. J. (2015) MicroRNA as type I interferon-regulated transcripts and modulators of the innate immune response. *Front. Immunol.* **6**, 334
37. Barroso-delJesus, A., Romero-López, C., Lucena-Aguilar, G., Melen, G. J., Sanchez, L.,

Ligero, G., Berzal-Herranz, A., and Menendez, P. (2008) Embryonic stem cell-specific miR302-367 cluster: human gene structure and functional characterization of its core promoter. *Mol. Cell Biol.* **28**, 6609-6619

38. Chen, X., Zhou, L., Peng, N., Yu, H., Li, M., Cao, Z., Lin, Y., Wang, X., Li, Q., Wang, J., She, Y., Zhu, S., Lu, M., Zhu, Y., and Liu, S. (2017) MicroRNA-302a suppresses influenza A virus–stimulated interferon regulatory factor-5 expression and cytokine storm induction. *J. Biol. Chem.* **292**, 21291-21303
39. Tatsuta, T., Model, K., and Langer, T. (2005) Formation of membrane-bound ring complexes by prohibitins in mitochondria. *Mol. Biol. Cell* **16**, 248-259
40. Artal-Sanz, M., and Tavernarakis, N. (2009) Prohibitin and mitochondrial biology. *Trends Endocrinol. Metab.* **20**, 394-401
41. Osman, C., Haag, M., Potting, C., Rodenfels, J., Dip, P.V., Wieland, F.T., Brügger, B., Westermann, B., and Langer, T. (2009) The genetic interactome of prohibitins: coordinated control of cardiolipin and phosphatidylethanolamine by conserved regulators in mitochondria. *J. Cell Biol.* **184**, 583-596
42. Zhang, W., Wang, G., Xu, Z-G., Tu, H., Hu, F., Dai, J., Chang, Y., Chen, Y., Lu, Y., Zeng, H., Cai, Z., Han, F., Xu, C., Jin, G., Sun, L., Pan, B-S., Lai, S-W., Hsu C-C., Xu, J., Chen, Z-Z., Li, H-Y., Seth, P., Hu, J., Zhang, X., Li, H., and Lin, H-K. (2019) Lactate is a natural suppressor of RLR signaling by targeting MAVS. *Cell* **178**, 176-189
43. Mills, E. L., Kelly, B., and O'Neill, L. A. J. (2017) Mitochondria are the powerhouses of immunity. *Nat. Immunol.* **18**, 488-498
44. Banoth, B., and Cassel, S. L. (2018) Mitochondria in innate immune signaling. *Transl. Res.* **202**, 52-68
45. Yasukawa, K., Oshiumi, H., Takeda, M., Ishihara, N., Yanagi, Y., Seya, T., Kawabata, S., and

Koshiba, T. (2009) Mitofusin 2 inhibits mitochondrial antiviral signaling. *Sci. Signal.* **2**, ra47

46. Bolstad, B.M., Irizarry, R. A., Astrand, M., and Speed, T.P. (2003) A comparison of normalization methods for high density oligonucleotide array data based on variance and bias. *Bioinformatics* **19**, 185-193
47. Gentleman, R.C., Carey, V. J., Bates, D. M., Bolstad, B., Dettling, M., Dudoit, S., Ellis, B., Gautier, L., Ge, Y., Gentry, J., Hornik, K., Hothorn, T., Huber, W., Iacus, S., Irizarry, R., Leisch, F., Li, C., Maechler, M., Rossini, A. J., Sawitzki, G., Smith, C., Smyth, G., Tierney, L., Yang, J. Y. H., and Zhang, J. (2004) Bioconductor: open software development for computational biology and bioinformatics. *Genome Biol.* **5**, R80
48. Quackenbush J. (2002) Microarray data normalization and transformation. *Nat. Genetics* **32**, 496-501
49. Yaku, K., Okabe, K., and Nakagawa, T. (2018) Simultaneous measurement of NAD metabolome in aged mice tissue using liquid chromatography tandem-mass spectrometry (LC/MS/MS). *Biomed. Chromatogr.* **32**, e4205
50. Yamamoto, M., Hikosaka, K., Mahmood, A., Tobe, K., Shojaku, H., Inohara, H., and Nakagawa, T. (2016) Nmnat3 is dispensable in mitochondrial NAD level maintenance in vivo. *PLoS One* **11**, e0147037
51. Saeed, A. I., Sharov, V., White, J., Li, J., Liang, W., Bhagabati, N., Braisted, J., Klapa, M., Currier, T., Thiagarajan, M., Sturn, A., Snuffin, M., Rezantsev, A., Popov, D., Ryltsov, A., Kostukovich, E., Borisovsky, I., Liu, Z., Vinsavich, A., Trush, V., and Quackenbush, J. (2003) TM4: a free, open-source system for microarray data management and analysis. *Biotechniques* **34**, 374-378

Abbreviations

The abbreviations used are: miRNA or miR, microRNA; IFN-β, interferon β; TNF-α, tumor necrosis factor α; RANTES, regulated on activation normal T-cell expressed and secreted; Toll-like receptor 3; RLR, retinoic acid-inducible gene I (RIG-I)-like receptor; MAVS, mitochondrial antiviral signaling protein; MOM, mitochondrial outer membrane; poly(I:C), polyinosinic-polycytidylic acid; SeV, Sendai virus; qPCR, quantitative PCR; HAU, hemagglutinin units; p.i., post-infection; HEK293, human embryonic kidney 293; IRF-3, interferon regulatory factor 3; DRP1, dynamin-related protein 1; MID49/51, mitochondrial dynamics protein 49/51; RAB32, Ras-related protein 32; SLC25A12, solute carrier family 25 member 12; MIM, mitochondrial inner membrane; PHB, prohibitin; IMS, mitochondrial intermembrane space; TBK-1, TANK-binding kinase 1; OCR, oxygen consumption rate; ECAR, extracellular acidification rate; MPC1, mitochondrial pyruvate carrier 1; BRET, bioluminescence resonance energy transfer; mtHSP70, mitochondrial heat shock protein 70; FCCP, carbonyl cyanide-*p*-trifluoromethoxyphenylhydrazone.

Table 1. Summary of miRNAs involved in the RLR-pathway and mitochondrial dynamics

miRNA	miRNA expression (fold per control)		luciferase activity	mitochondrial morphology
	poly(I:C) stimulation	SeV infection	IFN-β (fold % per control)	
hsa-miR-1250	229	2.5	16.1	normal tubular
hsa-miR-143	138	14.7	40.8	normal tubular
hsa-miR-302b-3p	4.3	2.9	3.5	strong fragmentation
hsa-miR-338-5p	3.1	5.0	36.7	normal tubular
hsa-miR-372	4.3	2.4	6.5	strong fragmentation
hsa-miR-410	70.1	110	186	normal tubular
hsa-miR-485-3p	287	212	45.6	normal tubular
hsa-miR-520f-3p	17.3	5.4	7.8	partial fragmentation
hsa-miR-922	16.3	13.0	71.5	normal tubular

Figure Legends

Figure 1. MicroRNAs that respond to RLR-mediated antiviral signaling. *A*, a log-log plot showing fold-change in miRNA expression (analyzed by TaqMan low-density array) in HEK293 cells transfected with poly(I:C) (10 μg for 24 h) versus Mock-transfected cells plotted against those of SeV-infection (16 hemagglutinin units (HAU)/mL for 24 h) ($n = 1$). The dashed box in the graph shows the significantly increased miRNA area (abundance ratio > 2), and the *inset* on the *top* shows the annotated miRNAs from the dashed box. *B*, activation of the IFN-β reporter (p125luc) in miRNA mimic-treated HEK293 cells (each, 10 nM concentration) transfected with 500 ng poly(I:C) for 24 h. NC (*left* in the graph), negative control mimic. Data shown represent mean values ± SD ($n = 3$). $^{*}P < 0.05$, $^{**}P < 0.01$, and $^{***}P < 0.001$. *C*, the indicated nine miRNA mimics were transfected in HeLa cells, and mitochondria in the cells were identified by stable expression of mitochondrially-targeted red fluorescent protein (12) by fluorescence microscopy. Scale bar, 10 μm. NC, negative control mimic. *D*, the kinetics of *IFN-β* and miR-302b expression in A549 cells with either SeV-infection (*top*) or poly(I:C)-transfection (*bottom*). The stimulated cells were collected at the indicated time-points (0, 6, 12, 24, and 36 h) and analyzed by qPCR. Both *GAPDH* and *U6* were used as internal controls. Data shown represent mean values ± SD ($n = 3$). $^{*}P < 0.05$ and $^{**}P < 0.01$. *E*, expression profiles of miR-302b detected by qPCR in three cell lines (HEK293, MRC-5, and HAP-1) post-transfection with 5 μg poly(I:C) 24 h later. *U6* was used as an internal control. Data shown represent mean values ± SD ($n = 3$). $^{*}P < 0.05$ and $^{***}P < 0.001$. *F*, the negative control (NC) or miR-302b mimic-transfected HEK293 cells were infected with SeV (4 HAU/mL) for 24 h, and the total RNAs from the cells were analyzed by qPCR for the expression of *IFN-β*, *RANTES*, *TNF-α*, and *GAPDH* (internal control). Data shown represent mean values ± SD ($n = 3$). $^{**}P < 0.01$ and $^{***}P < 0.001$. *G*, similar to *F*, except that the cells were stimulated with 2 μg poly(I:C) and

endogenous IRF-3 activation (phosphorylation) was detected by Western blotting. *H*, similar to *F*, except that the culture supernatants from cells were analyzed by ELISA to measure IFN-β production. N.D., not detected. Data shown represent mean values ± SD (n = 3). ***P < 0.001.

Figure 2. Both miR-302b and miR-372 are upregulated by triggering RLR-mediated signaling and act as inhibitors of the pathway. *A*, the kinetics of *IFN-β* and miR-372 expression in A549 cells transfected with poly(I:C) (5 μg). The stimulated cells were collected at the indicated time-points (0, 12, 24, and 36 h) and analyzed by qPCR. Both *GAPDH* and *U6* were used as internal controls. *B*, the expression profiles of miR-372 detected 24 h later by qPCR in three different cell lines (HEK293, MRC-5, and HAP-1) transfected with poly(I:C) (5 μg). *U6* was used as an internal control. *C*, Negative control mimic (NC) or miR-372 mimic-transfected HEK293 cells (~48 h) was infected with SeV (4 HAU/mL) for 24 h, and the total RNAs from the cells were analyzed by qPCR for the expression of *IFN-β*, *RANTES*, and *GAPDH* (internal control). *D*, similar to *C*, except that the miRNA mimic-treated cells were transfected with 2 μg poly(I:C) for 24 h, and the *IFN-β*, *RANTES*, and *GAPDH* (internal control) mRNA expression was measured by qPCR. *E*, similar to *D*, except that the culture supernatants from A549 cells were analyzed by ELISA to measure IFN-β production. *F*, similar to *E*, except that A549 cells were infected with SeV (4 HAU/mL). *G*, activation of the IFN-β (p125luc) or NF-κB (pELAM) reporters at 24 h in miRNA mimic-treated HEK293 cells transfected with either encoded MAVS or RIG-I$^{1\text{-}250}$ expression plasmids. All data shown represent mean values ± SD (n = 3). *P < 0.05, **P < 0.01, and ***P < 0.001.

Figure 3. Both endogenous miR-302b and miR-372 regulate RLR-mediated signal

transduction. *A* and *B*, HEK293 (*A*) or HAP-1 (*B*) cells were transfected with either the negative control (NC) or indicated miRNA inhibitors and 48 h later, the cells were re-transfected with 2 μg poly(I:C) for 24 h, and the total RNAs from the cells were analyzed by qPCR for the expression of *IFN-β* (*left*) or the culture supernatants from the cells were analyzed by ELISA to measure IFN-β production (*right*). *GAPDH* was used as an **i**nternal control for the qPCR experiments. N.D., not detected. Data shown represent mean values ± SD (n = 3). *$P < 0.05$, **$P < 0.01$, and ***$P < 0.001$.

Figure 4. miR-302b promotes mitochondrial fission through a DRP1-dependent pathway. *A*, HeLa cells were transfected with either negative control (NC) or miR-302b mimics, and the mitochondrial morphology of the transfected cells was monitored 72 h later by immunofluorescence microscopy. Mitochondria in the cells were stained with an antibody against mtHSP70. The presence of an miR-302b specific inhibitor rescued its defects in mitochondrial tubular networks (*right*, miR-302b + inhibitor). Each *inset* depicts a magnified image of the dashed-boxed area. Scale bar, 10 μm (*inset*, 5 μm). *B*, quantification of mitochondrial morphology in *A*. Cells were scored as one of four morphologic categories as depicted in the *inset*, and at least 200 cells were scored. Data shown represent mean values ± SD (n = 3). *C*, total RNAs were isolated from HEK293 cells post-transfection with either negative control (NC) or miR-302b mimics for 72 h and microarray analysis was performed (n = 1). The heat map (*left*) compared the expression profile of mitochondrial dynamics-related genes, and was generated by MeV software (51). The color indicates the distance from the median of each row. The *right* graph shows the gene expression profiles of the cells transfected either with miR-302b or miR-372 mimics for 72h and analyzed by qPCR. NC, negative control mimic. The qPCR data shown represent mean values ± SD (n = 3). *$P < 0.05$, **$P < 0.01$,

and ***$P < 0.001$. *D*, HEK293 cells were transfected with either plasmid, psiCHECK-2 (empty), or psiCHECK-2 that cloned a 3'-UTR region of *RAB32* (110-140), together with a miR-302b mimic. The transfected cells were analyzed 24 h later for reporter gene-dependent luciferase activity. *Top*, predicted base-pairing between miR-302b-3p and the *RAB32* target, and the positions of paired sites are indicated by the red bars. Data shown represent mean values ± SD ($n = 3$). ***$P < 0.001$. *E*, HEK293 cells were transfected with the negative control (NC) or miRNA mimics, and the whole cells lysates were analyzed by Western blotting with an antibody against RAB32 (*left*). The band intensity of RAB32 was measured with QuantiStudio, and normalized to the intensity of β-actin (*right*) (data shown represent mean values ± SD ($n = 3$)). **$P < 0.01$. *F*, HeLa cells were transfected with the negative control (NC) or miRNA mimics and 72 h after transfection, DRP1 phosphorylation (Ser^{637}) levels of forskolin-stimulated cells were analyzed 72 h later by Western blotting (*left*). The band intensity of pDRP1 (S637) was measured and normalized to the intensity of GAPDH (*right*) (data shown represent mean values ± SD ($n = 5$)). ***$P < 0.001$. *G*, similar to *E*, except that the expression levels of MID49 and MID51 were analyzed by Western blotting. Data shown represent mean values ± SD ($n = 3$). *$P < 0.05$. *H*, similar to *E*, except that the endogenous DRP1 localization in cytosolic (Cyto) and mitochondrial (Mt) fractions isolated from the cells was analyzed by Western blotting. Data shown represent mean values ± SD ($n = 3$). ***$P < 0.001$. *I*, HEK293 cells were transfected with either the negative control (NC) or miRNA mimics, together with the *DRP1* siRNA (vs *siControl*) for 48 h. The transfected cells were then stimulated with poly(I:C)-delivery into cells, and the expression of *IFN-β*, *RANTES*, and *GAPDH* (internal control) was measured by qPCR post poly(I:C) transfection (2 μg). Data shown represent mean values ± SD ($n = 3$). *$P < 0.05$, **$P < 0.01$, and ***$P < 0.001$.

Figure 5. Involvement of miR-302b and miR-372 in mitochondrial dynamics. *A*, HeLa cells were transfected with either negative control (NC) or miR-372 mimics, and the mitochondrial morphology of the transfected cells was monitored 72 h later by immunofluorescence microscopy. Mitochondria in the cells were stained with an antibody against mtHSP70. The right image shows that the presence of a miR-372 specific inhibitor rescued its defects in mitochondrial tubular networks (miR-372 + inhibitor). Each inset depicts the magnified image of the dashed-boxed area. Scale bar, 10 μm (*inset*, 5 μm). *B*, quantification of mitochondrial morphology in *A*. Cells were scored as one of four morphologic categories as depicted in the inset, and at least 200 cells were scored. *C*, HEK293 cells were transfected with either plasmid, psiCHECK-2 (empty) or psiCHECK-2, that cloned a 3'-UTR region of *RAB32* (110-140), together with the miR-372 mimic. Transfected cells were analyzed 24 h later for reporter gene-dependent luciferase activities. Top, predicted base-pairing between miR-372-3p and the RAB32 target, and the positions of paired sites are indicated by the red bars. *D*, total RNAs from HEK293 cells transfected with either the negative control (NC) or miR-302b mimic (~72 h) were analyzed by qPCR to confirm the expression of *RAB32*, *MID49*, and *MID51*. *GAPDH* was used as the internal control. *E*, similar to *D*, except that HEK293 cells were transfected with the miR-372 mimic. *F*, HeLa cells were transfected with the negative control (*siControl*) or *RAB32* siRNA for 72 h, and the DRP1 phosphorylation (Ser637) levels of forskolin-stimulated cells were analyzed by Western blotting (*left*). The band intensity of pDRP1 was measured with QuantiStudio, and normalized by the intensity of GAPDH (*right*). *G*, mitochondrial morphologies in HeLa cells transfected with either the negative control (NC) or miR-302b mimics, together with the *DRP1* siRNA for 72 h. Each *inset* depicts the magnified image of the dashed-boxed area. Scale bar, 10 μm (*inset*, 5 μm). All data shown represent mean values ± SD ($n = 3$). *$P < 0.05$ and ***$P < 0.001$.

Figure 6. miR-302b modulates SLC25A12 expression, which is involved in attenuating the mitochondrial-mediated antiviral response. *A*, representative MA plot of the microarray data. The X-axis represents the $\log_2$ transform of the microarray signals, and the y-axis represents the $\log_2$ transform of the fold-change of each gene in HEK293 cells transfected between negative control and miR-302b mimics (n = 1). Expression changes greater or less than 2-fold are considered as hits and are indicated as red and blue dots, respectively. Genes annotated as known *SLC25* family members are indicated in black, and the *inset* on the *right* shows the highlight of only the *SLC25* family position in which the *SLC25A12* is indicated in red. *B*, HEK293 cells were transfected with either psiCHECK-2 (empty) or psiCHECK-2 that contained a 3'-UTR region of *SLC25A12* (251-280), together with miR-302b mimic. Transfected cells were analyzed 24 h later for reporter gene-dependent luciferase activities. *Top*, predicted base-pairing between miR-302b-3p and the target gene, and the positions of paired sites are indicated by the red bars. Data shown represent mean values ± SD (n = 3). ***P < 0.001. *C*, HEK293 cells were transfected with the negative control (NC) or miR-302b mimics, and whole cell lysates were analyzed 72 h later by Western blotting with an antibody against SLC25A12 (*top*). Band intensity was measured with ImageQuant TL, and normalized to the intensity of β-actin (*bottom*) (data shown represent mean values ± SD (n = 3)). *P < 0.05. *D*, siRNA-treated HEK293 cells (*siSLC25A12*) were transfected with 2 μg poly(I:C) for 24 h, and the total RNA from the cells was analyzed by qPCR for the expression of *IFN-β*, *RANTES*, and *GAPDH* (internal control). Data shown represent mean values ± SD (n = 3). **P < 0.01. The efficiency of SLC25A12 knockdown was confirmed by Western blots analysis with an antibody against SLC25A12 (*bottom*). *E*, *SLC25A12* knockout and its parental (WT) HAP-1 cell lines were infected with SeV (4 HAU/mL) for 24 h, and IFN-β production was measured by ELISA. N.D., not detected. Data shown represent mean values ± SD (n = 3). ***P < 0.001.

Figure 7. SLC25A12 involvement in mitochondrial-mediated antiviral signaling. *A*, HEK293 cells were transfected with either psiCHECK-2 (empty) or psiCHECK-2 that cloned a 3'-UTR region of *SLC25A12* (251-280), together with a miR-372 mimic. The transfected cells were analyzed 24 h later for reporter gene-dependent luciferase activities. *Top*, predicted base-pairing between miR-372-3p and the target gene, and the positions of the paired sites are indicated by the red bars. *B*, HEK293 cells were transfected with either the negative control (*siControl*) or *SLC25A12* siRNA. Forty-eight hours later, siRNA-treated cells were transfected with the IFN-β (p125luc) reporter plasmid together with plasmids encoding MAVS, RIG-I$^{1\text{-}250}$, or TBK1, and reporter gene-dependent luciferase activities were analyzed 24 h post transfection. All data shown represent mean values ± SD (n = 3). N.S., not significant, and ***$P < 0.001$.

Figure 8. SLC25A12 associates with the mitochondrial antiviral signaling protein MAVS. *A*, interaction of endogenous SLC25A12 with MAVS and PHB complexes. Lysates of HEK293 cells (*right*) were subjected to immunoprecipitation (IP, *left*) with anti-SLC25A12 antibody or control IgG followed by analysis of Western blots with antibodies against MAVS, PHB1, and PHB2. *B*, HEK293 cells were co-transfected with the indicated combinations of plasmids encoding HA-tagged MAVS and Myc-tagged SLC25A12 variants (*top*). Western blots of samples immunoprecipitated (IP) with an anti-Myc or post-nuclear cell lysates (Lysate) were analyzed by immunoblotting (IB) with either the anti-HA or the anti-Myc antibodies. *C*, immunofluorescence microscopy of HeLa cells transfected with a plasmid encoding Myc-tagged SLC25A12. Cells were visualized with endogenous MAVS (Alexa Fluor 488, green) and SLC25A12 (Cy3, red). Scale bar, 10 μm. *D*, the interaction between PHB1 and SLC25A12. A total of 1183 proteins re-analyzed using our previous PHB1 interactors (28) were plotted

according to the abundance ratios (log_2) of PHB1/control against individual proteins (Protein index) sorted by their ratios in ascending order. Interactions, such as those of PHB1 and CLPB, were confirmed as a positive control. *E*, the *SLC25A12* knockout (orange) or WT (black) HAP-1 cells were each co-transfected with 10 ng NLuc-MAVS expression plasmid with increasing amounts (0-100 ng) of Venus-tagged MAVS plasmid and analyzed 24 h later using a BRET saturation assay (30). Data shown represent mean values ± SD ($n = 3$). *$P < 0.05$, **$P < 0.01$, and ***$P < 0.001$. *F*, similar to *E*, except that the miRNA mimic-treated HEK293 cells were used. Data shown represent mean values ± SD ($n = 3$). *$P < 0.05$, **$P < 0.01$, and ***$P < 0.001$.

Figure 9. miR-302b targets SLC25A12 to disrupt mitochondrial metabolism linked to the antiviral responses. *A*, NAD and NADH levels (pmol/10^6 cells) in HEK293 cells transfected with miR-302b mimic were analyzed 72 h later by LC-MS/MS. The right graph shows the NAD/NADH ratio. N.S., not significant. Data shown represent mean values ± SD ($n = 3$). ***$P < 0.001$. *B*, mitochondria-related metabolites in the miR-302b mimic-transfected HEK293 cells analyzed 72 h later by GC/MS. The aspartate, malate, and pyruvate levels were each significantly decreased, whereas the lactate level was increased. Data shown represent mean values ± SD ($n = 3$). **$P < 0.01$ and ***$P < 0.001$. *C*, oxygen consumption rate (OCR) of HEK293 cells transfected with the miR-302b mimic (± inhibitor) measured using a Seahorse XFe96 Analyzer. *Inset*: basal OCR of each transfected cell. The injection order of oligomycin (Oligo), FCCP, and antimycin A/rotenone (Ant A/ Rot) is indicated. Data shown represent mean values ± SD ($n = 5$). ***$P < 0.001$. *D*, the extracellular acidification rate (ECAR) of HEK293 cells transfected with the miR-302b mimic (± inhibitor) was measured using the Seahorse XFe96 Analyzer. Data shown represent mean values ± SD ($n = 5$). ***$P < 0.001$. *E*, similar to *C*,

except that the representative respiration of the *SLC25A12* knockout and its WT HAP-1 cells was measured. Data shown represent mean values ± SD ($n = 5$). ***$P < 0.001$. *F*, siRNA-treated HEK293 cells (*siSLC25A12*) were transfected with 2 μg poly(I:C) for 24 h, and the total RNA from the cells was analyzed by qPCR for the expression of *IFN-β*, *RANTES*, and *GAPDH* (internal control). At the time of the poly(I:C) transfection, either pyruvate (Pyr, 2.5 mM) or aspartate (Asp, 10 mM) was added to the medium of the *siSLC25A12*-treated cells. Data shown represent mean values ± SD ($n = 3$). **$P < 0.01$ and ***$P < 0.001$. *G*, model of miRNAs that control RLR-mediated antiviral signaling. Cellular innate immune responses to RNA virus infection result in the rapid activation of signaling molecules including MAVS oligomerization (*inset*) and the formation of signalosomes on the MOM, ultimately facilitating the RLR signaling pathway (①). In this process, we assume that SLC25A12, as a part of the PHB interactome (*inset*, highlighted with blue background) (28), interacts with MAVS in mitochondria that have a critical role in MAVS oligomerization. At longer times post-infection (~24 h), miR-302b (and also miR-372) is upregulated in the cells, which promotes mitochondrial fission through the DRP1-dependent pathway and also impairs mitochondrial metabolism (②). We propose that the miRNAs undergo sequential negative regulations following viral infection, a process that is critical for terminating excess RLR signaling.

Figure 10. miR-302b also regulates MPC1 expression, which marginally attenuates mitochondrial metabolism. *A*, oxygen consumption rate (OCR) for HEK293 cells transfected with a miR-372 mimic (± inhibitor) measured using a Seahorse XFe96 Analyzer ($n = 5$). *Inset*: basal OCR of each transfected cell. The injection order of oligomycin (Oligo), FCCP, and antimycin A/rotenone (Ant A/ Rot) is indicated. The cells transfected with the negative control (NC) miRNA mimic are the same as those shown in Fig. 9C. *B*, similar to *A*, except that HEK293

cells were treated with siRNAs against *SLC25A12* or *MPC1*. *C*, similar to *A*, except that the representative respiration of the *SLC25A12* knockout HAP-1 cells was measured with or without supplying pyruvate (Pyr, 2.5 mM) or aspartate (Asp, 10 mM). *D*, HEK293 cells were transfected with either psiCHECK-2 (empty) or psiCHECK-2 that cloned a 3'-UTR region of *MPC1* (311-340), together with the miR-302b mimic. The transfected cells were analyzed 24 h later for reporter gene-dependent luciferase activities. Top, predicted base-pairing between miR-302b-3p and the target gene, and the positions of paired sites are indicated by the red bars. *E*, HEK293 cells were transfected with the negative control (NC) or miR-302b mimics, and whole cells lysates were analyzed 72 h later by Western blotting with an antibody against MPC1 (*left*). The band intensity was measured with ImageQuant TL, and normalized to the intensity of β-actin (*right*). The β-actin blot is the same panel as it shown in Fig. 6C because we shared the same whole cells lysates of HEK293 cells that were transfected with the negative control (NC) or miR-302b mimics. All data shown represent mean values ± SD ($n = 3$). *$P < 0.05$, **$P < 0.01$, and ***$P < 0.001$.

Figure 1

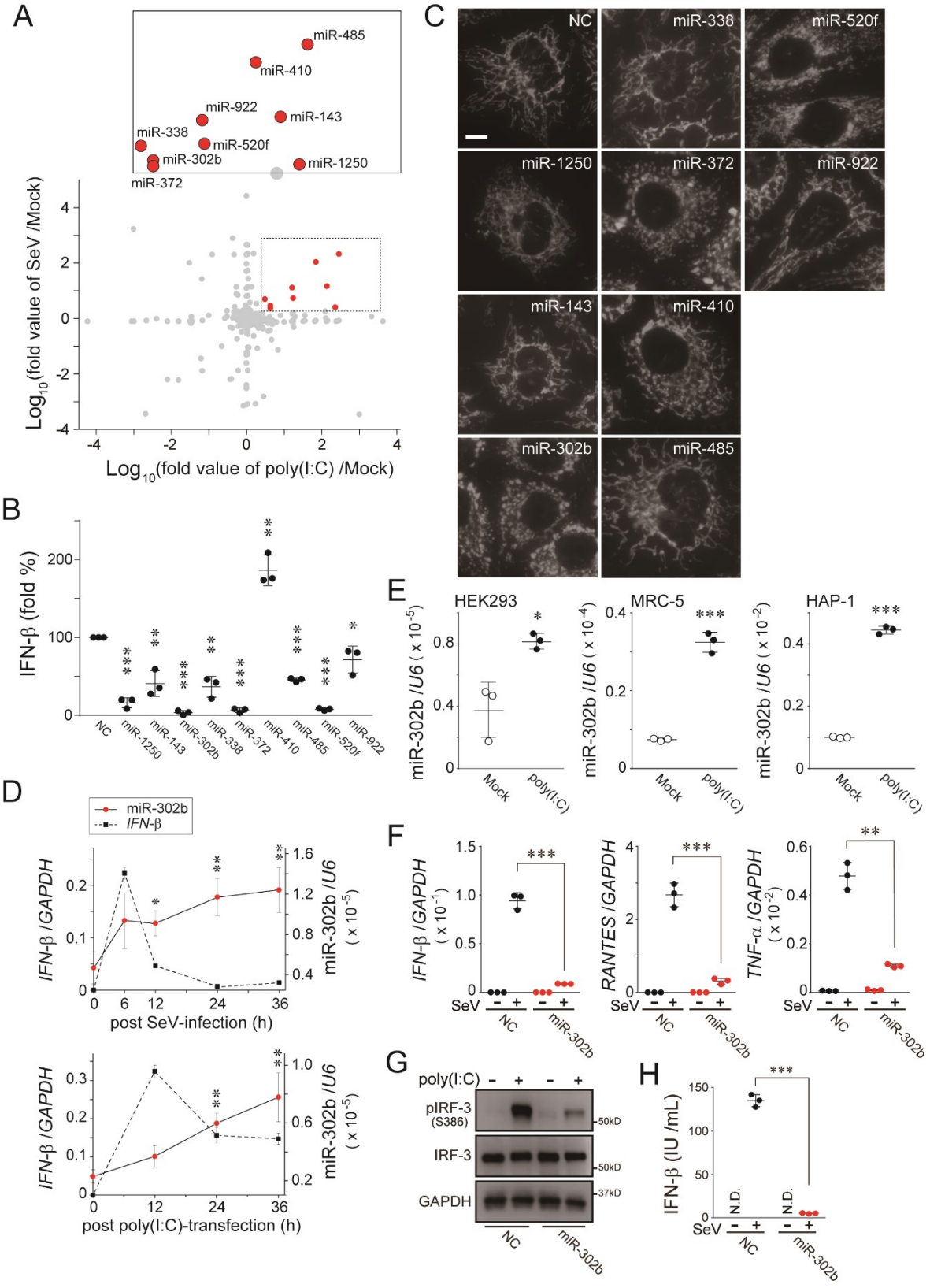
A
miR-485
miR-410
miR-922
miR-143
miR-338
miR-520f
miR-302b
miR-1250
miR-372
Log10(fold value of SeV /Mock)
Log10(fold value of poly(I:C) /Mock)
B
IFN-β (fold %)
NC
miR-1250
miR-143
miR-302b
miR-338
miR-372
miR-410
miR-485
miR-520f
miR-922
C
NC
miR-338
miR-520f
miR-1250
miR-372
miR-922
miR-143
miR-410
miR-302b
miR-485
D
miR-302b
IFN-β
IFN-β /GAPDH
miR-302b /U6 (x 10-5)
post SeV-infection (h)
post poly(I:C)-transfection (h)
E
HEK293
MRC-5
HAP-1
miR-302b /U6 (x 10-5)
miR-302b /U6 (x 10-4)
miR-302b /U6 (x 10-2)
Mock
poly(I:C)
F
IFN-β /GAPDH (x 10-1)
RANTES /GAPDH
TNF-α /GAPDH (x 10-2)
SeV
NC
miR-302b
G
poly(I:C)
pIRF-3 (S386)
IRF-3
GAPDH
50kD
50kD
37kD
H
IFN-β (IU /mL)
N.D.
N.D.

Figure 2

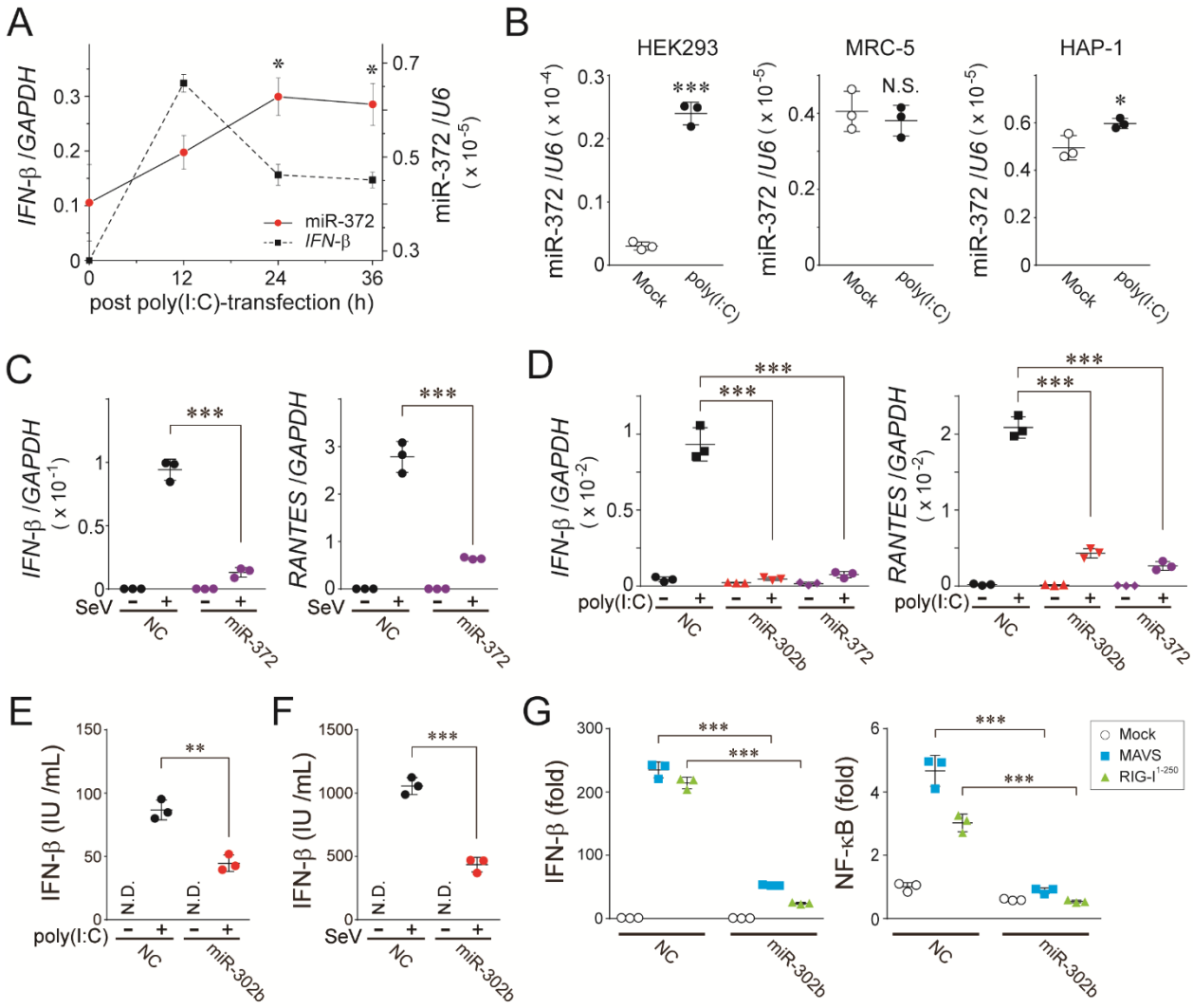
A
IFN-β /GAPDH
miR-372 /U6 (x 10-5)
miR-372
IFN-β
post poly(I:C)-transfection (h)
B
HEK293
MRC-5
HAP-1
miR-372 /U6 (x 10-4)
miR-372 /U6 (x 10-5)
N.S.
Mock
poly(I:C)
C
IFN-β /GAPDH (x 10-1)
RANTES /GAPDH
SeV
NC
miR-372
D
IFN-β /GAPDH (x 10-2)
RANTES /GAPDH (x 10-2)
poly(I:C)
NC
miR-302b
miR-372
E
IFN-β (IU /mL)
N.D.
poly(I:C)
NC
miR-302b
F
IFN-β (IU /mL)
SeV
G
IFN-β (fold)
NF-κB (fold)
Mock
MAVS
RIG-I1-250

Figure 3

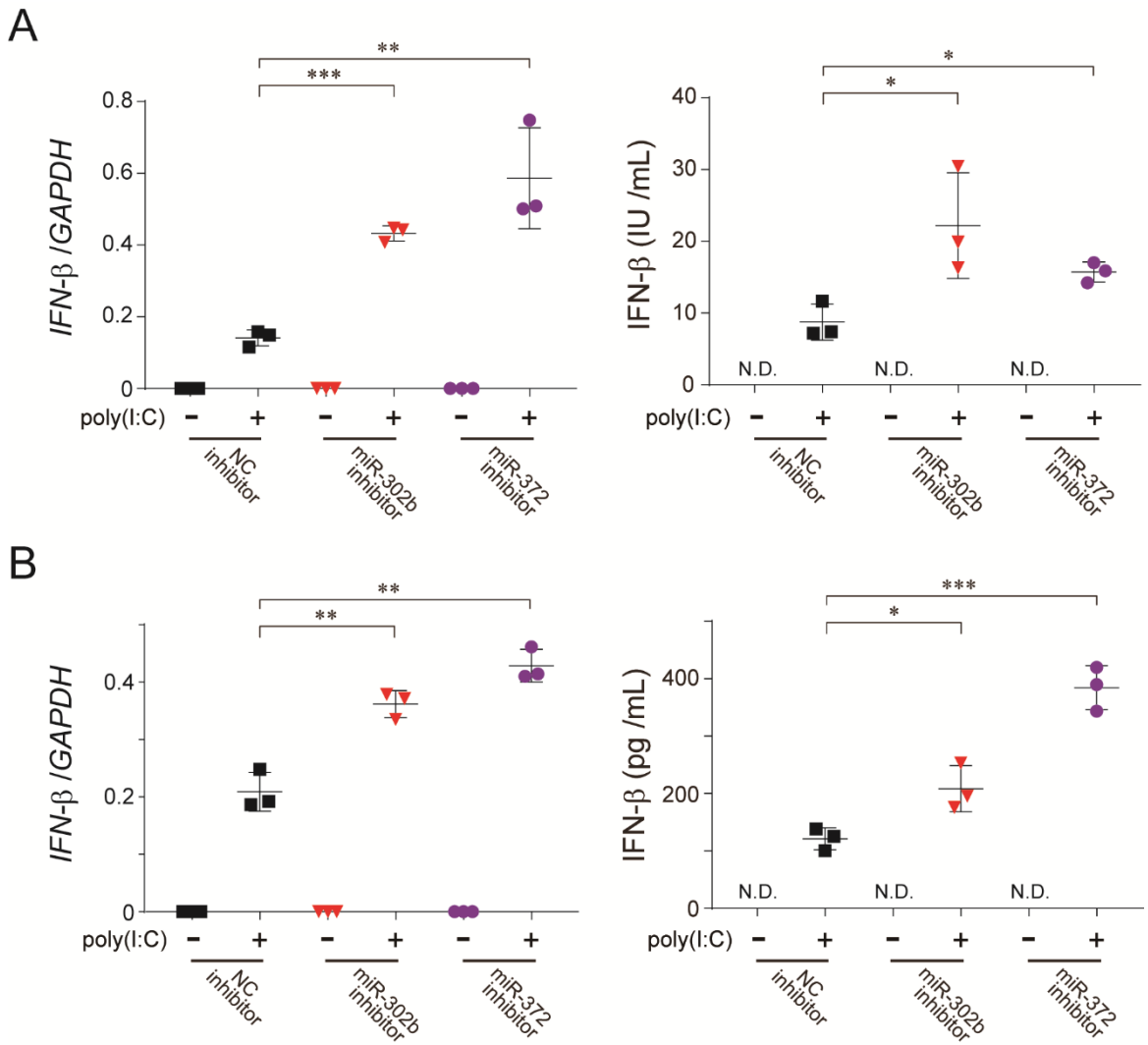
A
IFN-β /GAPDH
0.8
0.6
0.4
0.2
0
**
***
poly(I:C) - + - + - +
NC inhibitor
miR-302b inhibitor
miR-372 inhibitor
IFN-β (IU /mL)
40
30
20
10
0
*
*
N.D.
N.D.
N.D.
B
IFN-β /GAPDH
0.4
0.2
0
**
**
IFN-β (pg /mL)
400
200
0
***
*
N.D.
N.D.
N.D.

Figure 4

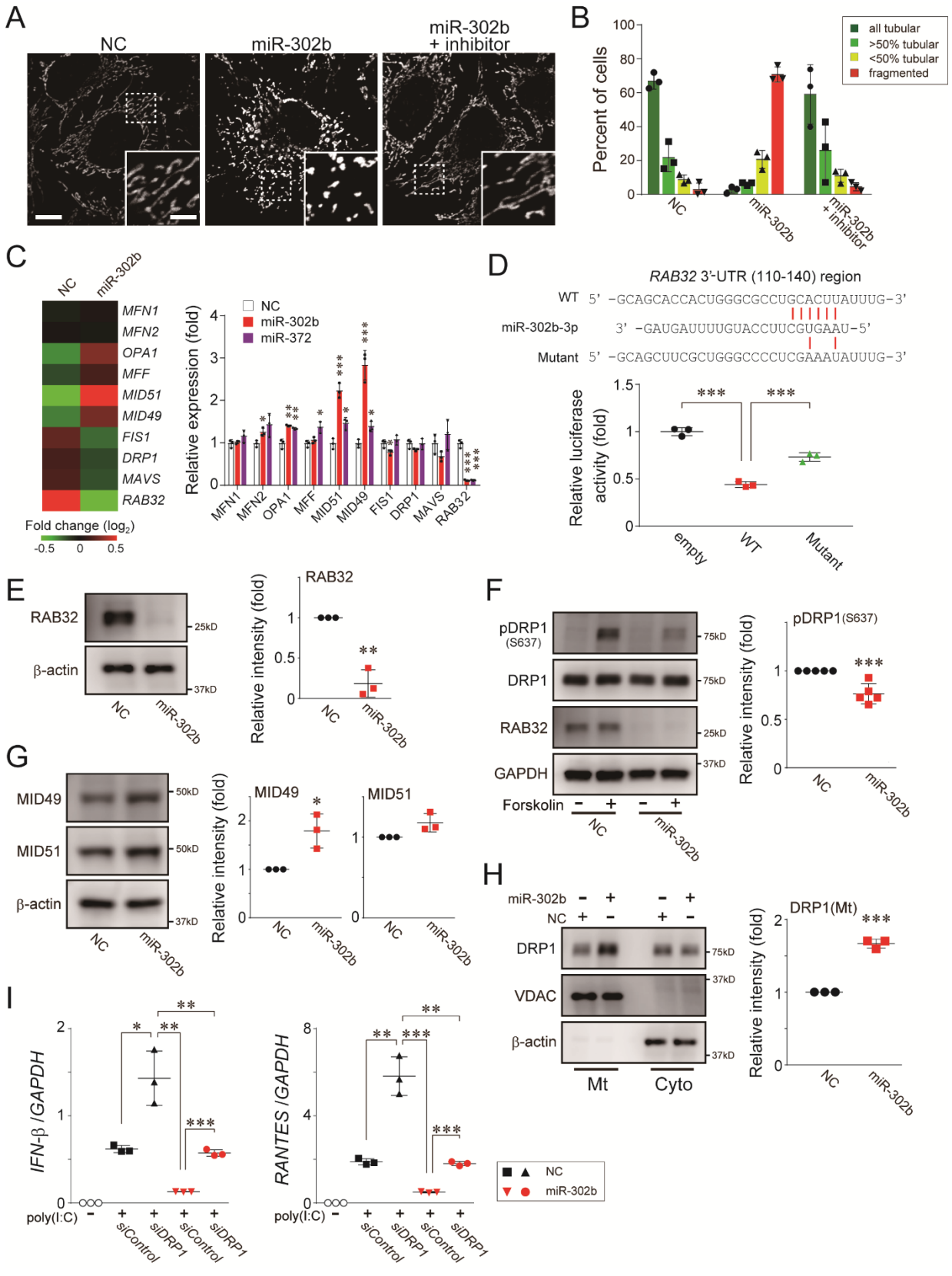
A
NC
miR-302b
miR-302b + inhibitor
B
Percent of cells
all tubular
>50% tubular
<50% tubular
fragmented
NC
miR-302b
miR-302b + inhibitor
C
NC
miR-302b
MFN1
MFN2
OPA1
MFF
MID51
MID49
FIS1
DRP1
MAVS
RAB32
Fold change (log2)
-0.5 0 0.5
Relative expression (fold)
NC
miR-302b
miR-372
D
RAB32 3'-UTR (110-140) region
WT 5' -GCAGCACCACUGGGCGCCUGCACUUAUUUG-3'
miR-302b-3p 3' -GAUGAUUUUGUACCUUCGUGAAU-5'
Mutant 5' -GCAGCUUCGCUGGGCCCCUCGAAAUAUUUG-3'
Relative luciferase activity (fold)
empty
WT
Mutant
E
RAB32
β-actin
25kD
37kD
Relative intensity (fold)
F
pDRP1 (S637)
DRP1
RAB32
GAPDH
75kD
25kD
37kD
Forskolin
pDRP1(S637)
G
MID49
MID51
β-actin
50kD
37kD
H
miR-302b
NC
DRP1
VDAC
β-actin
75kD
37kD
Mt
Cyto
DRP1(Mt)
I
IFN-β /GAPDH
RANTES /GAPDH
poly(I:C)
siControl
siDRP1
NC
miR-302b

Figure 5

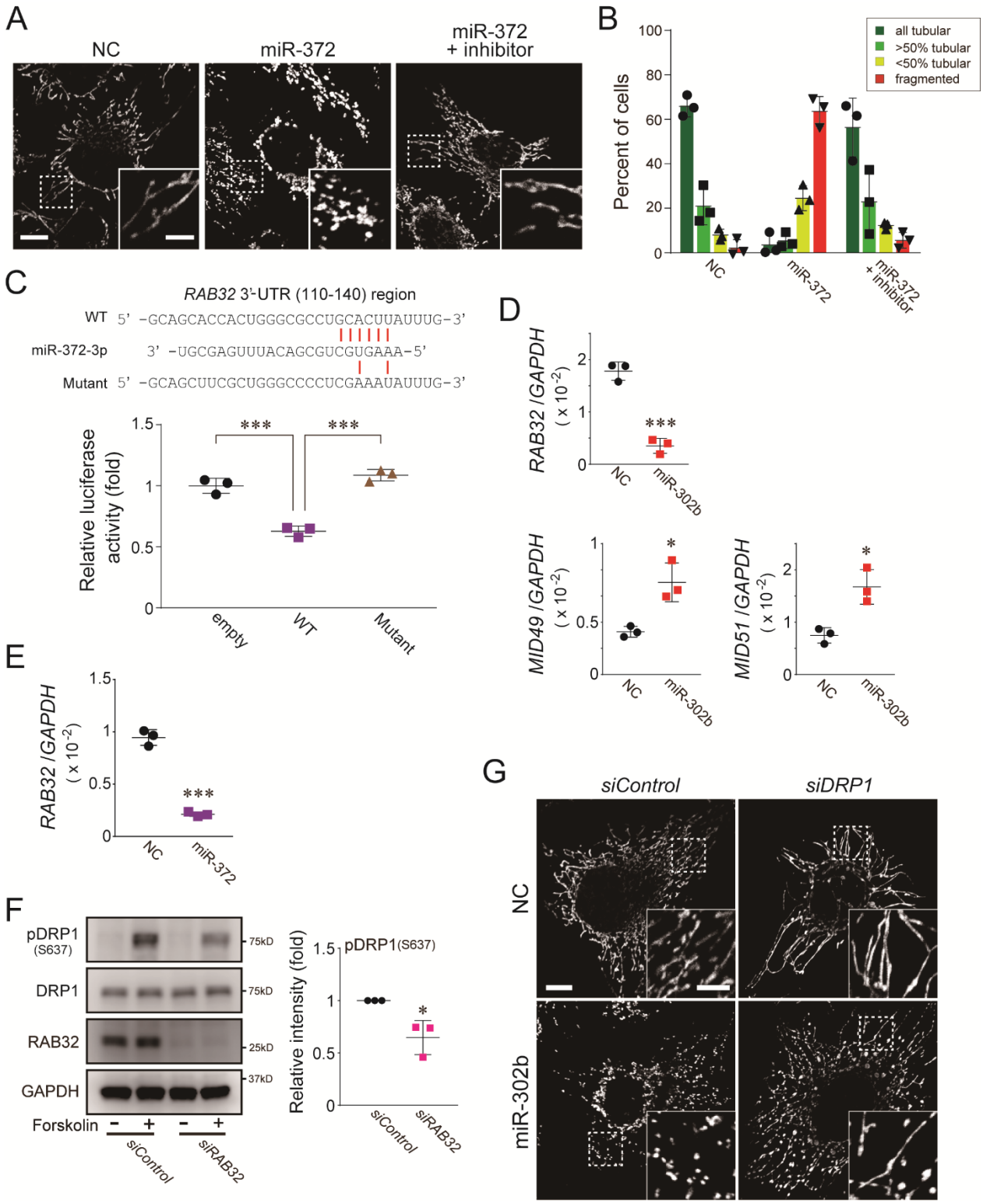
A
NC
miR-372
miR-372
+ inhibitor
B
all tubular
>50% tubular
<50% tubular
fragmented
Percent of cells
NC
miR-372
miR-372
+ inhibitor
C
RAB32 3'-UTR (110-140) region
WT 5' -GCAGCACCACUGGGCGCCUGCACUUAUUUG-3'
miR-372-3p 3' -UGCGAGUUUACAGCGUCGUGAAA-5'
Mutant 5' -GCAGCUUCGCUGGGCCCCUCGAAAUAUUUG-3'
Relative luciferase activity (fold)
empty
WT
Mutant
D
RAB32 /GAPDH
MID49 /GAPDH
MID51 /GAPDH
NC
miR-302b
E
RAB32 /GAPDH
NC
miR-372
F
pDRP1 (S637)
DRP1
RAB32
GAPDH
Forskolin
siControl
siRAB32
Relative intensity (fold)
G
siControl
siDRP1
NC
miR-302b

Figure 6

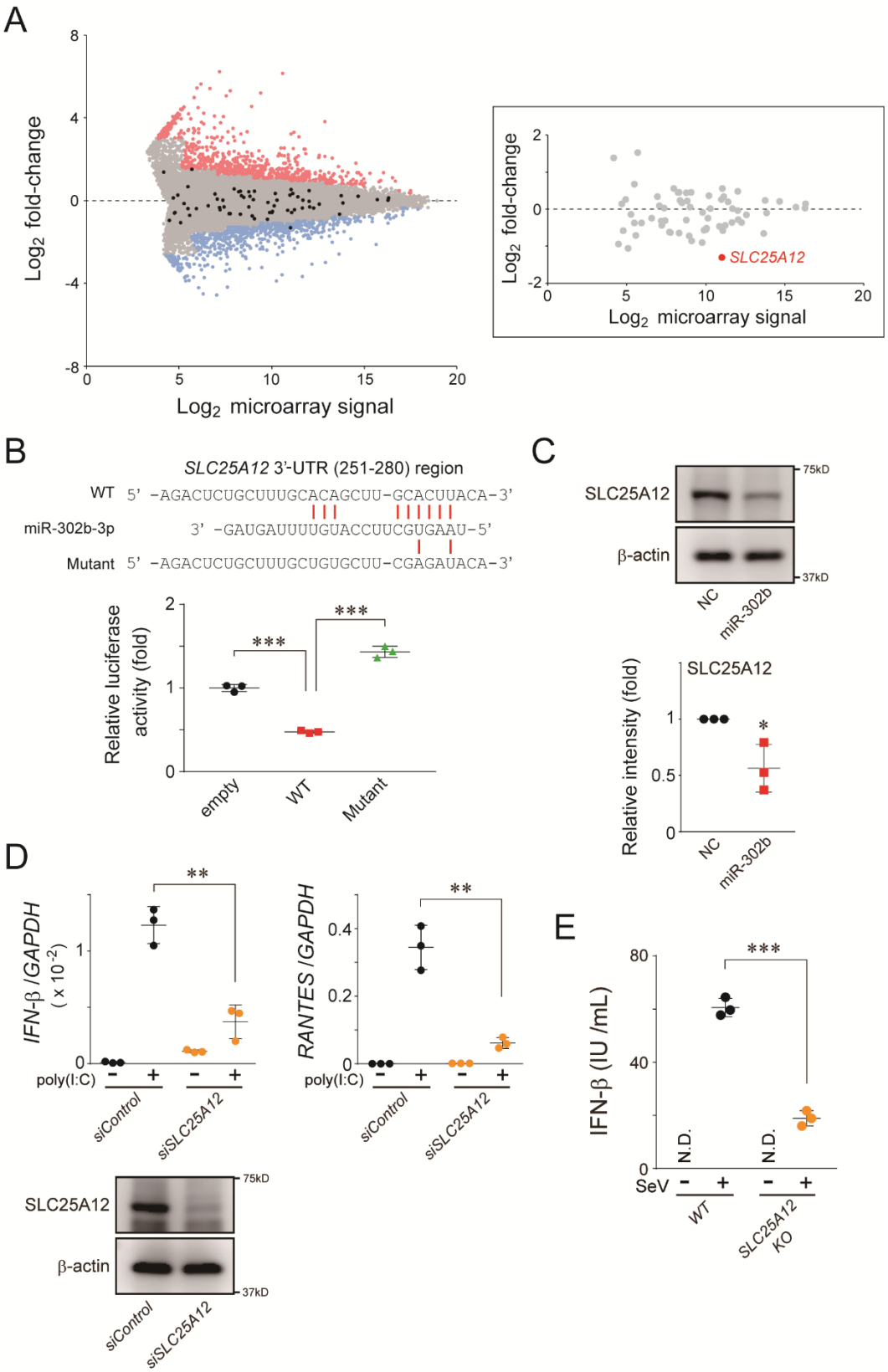
A
Log2 fold-change
Log2 microarray signal
SLC25A12
B
SLC25A12 3'-UTR (251-280) region
WT 5' -AGACUCUGCUUUGCACAGCUU-GCACUUACA-3'
miR-302b-3p 3' -GAUGAUUUUGUACCUUCGUGAAU-5'
Mutant 5' -AGACUCUGCUUUGCUGUGCUU-CGAGAUACA-3'
Relative luciferase activity (fold)
empty
WT
Mutant
C
SLC25A12
β-actin
75kD
37kD
NC
miR-302b
Relative intensity (fold)
D
IFN-β /GAPDH (x 10-2)
RANTES /GAPDH
poly(I:C)
siControl
siSLC25A12
E
IFN-β (IU /mL)
N.D.
SeV
WT
SLC25A12 KO

Figure 7

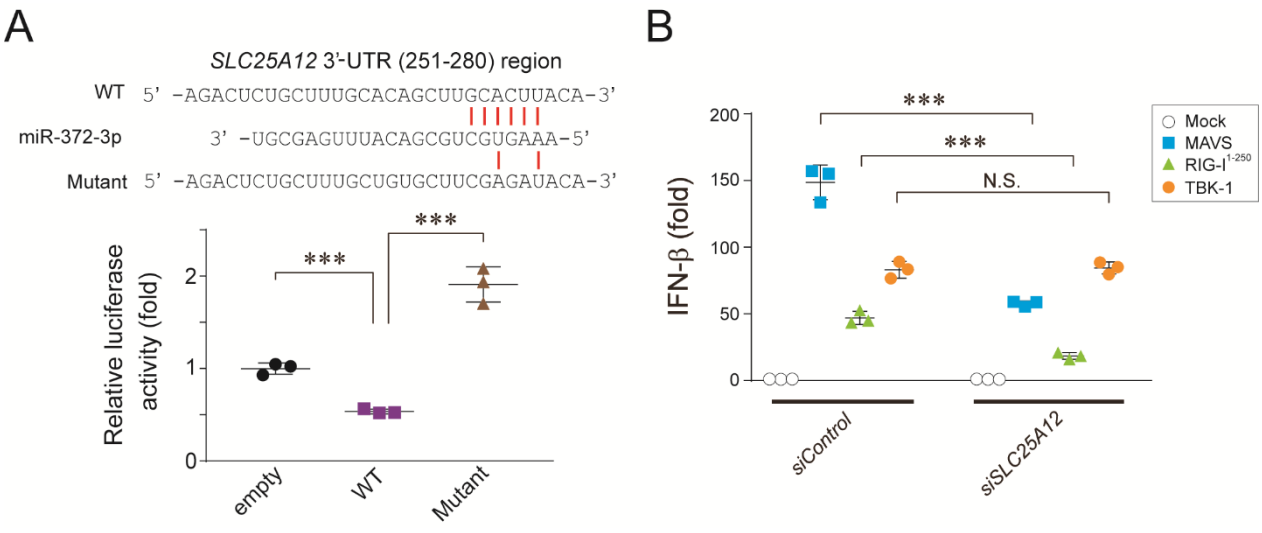
A
SLC25A12 3'-UTR (251-280) region
WT 5' -AGACUCUGCUUUGCACAGCUUGCACUUACA-3'
miR-372-3p 3' -UGCGAGUUUACAGCGUCGUGAAA-5'
Mutant 5' -AGACUCUGCUUUGCUGUGCUUCGAGAUACA-3'
Relative luciferase activity (fold)
***
***
empty
WT
Mutant
B
IFN-β (fold)
***
***
N.S.
Mock
MAVS
RIG-I1-250
TBK-1
siControl
siSLC25A12

Figure 8

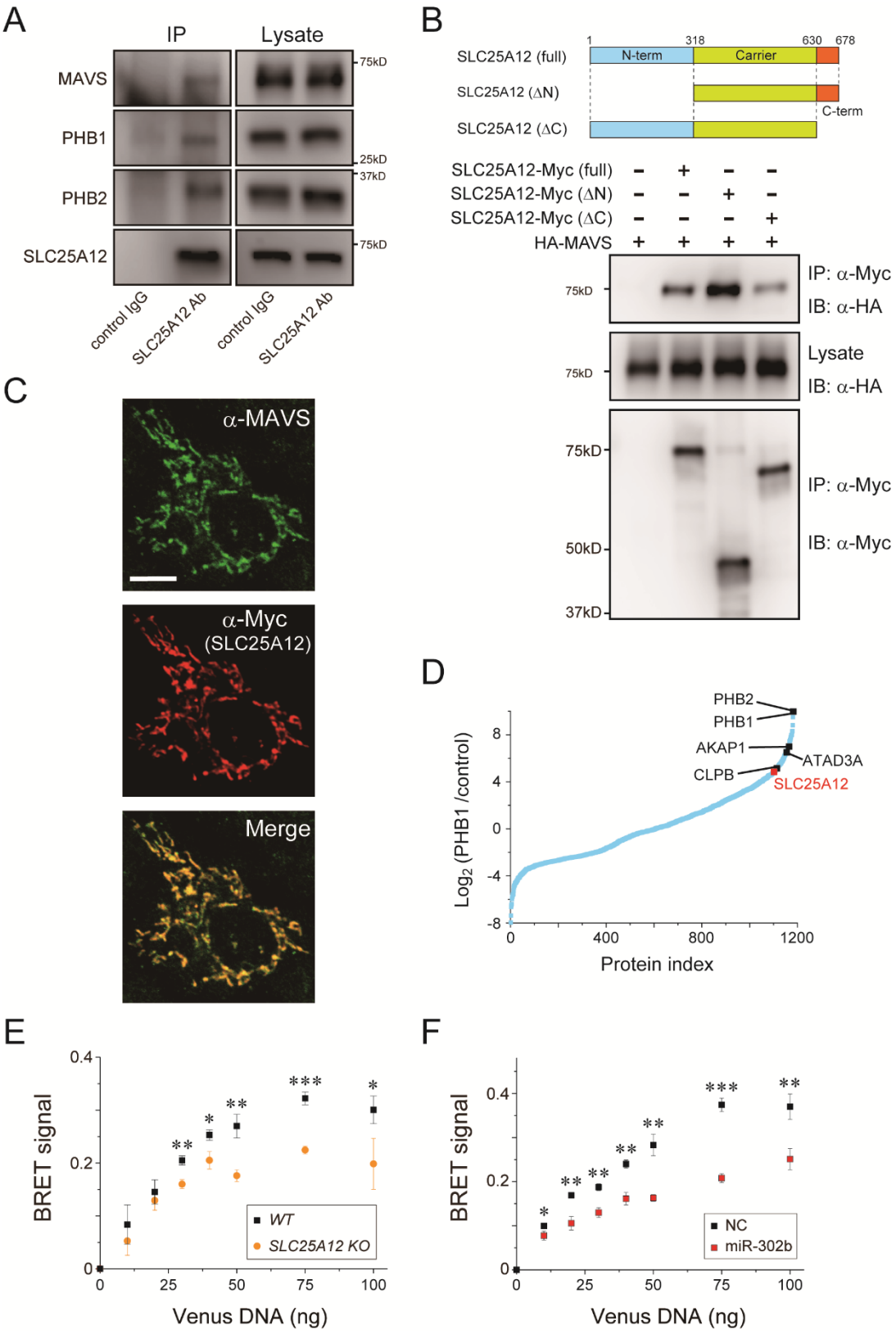
A
IP
Lysate
MAVS
PHB1
PHB2
SLC25A12
75kD
25kD
37kD
75kD
control IgG
SLC25A12 Ab
control IgG
SLC25A12 Ab
B
SLC25A12 (full)
SLC25A12 (ΔN)
SLC25A12 (ΔC)
1
318
630
678
N-term
Carrier
C-term
SLC25A12-Myc (full)
SLC25A12-Myc (ΔN)
SLC25A12-Myc (ΔC)
HA-MAVS
IP: α-Myc
IB: α-HA
Lysate
IB: α-HA
IP: α-Myc
IB: α-Myc
75kD
50kD
37kD
C
α-MAVS
α-Myc
(SLC25A12)
Merge
D
PHB2
PHB1
AKAP1
ATAD3A
CLPB
SLC25A12
Log2 (PHB1 /control)
Protein index
E
BRET signal
WT
SLC25A12 KO
Venus DNA (ng)
F
BRET signal
NC
miR-302b
Venus DNA (ng)

Figure 9

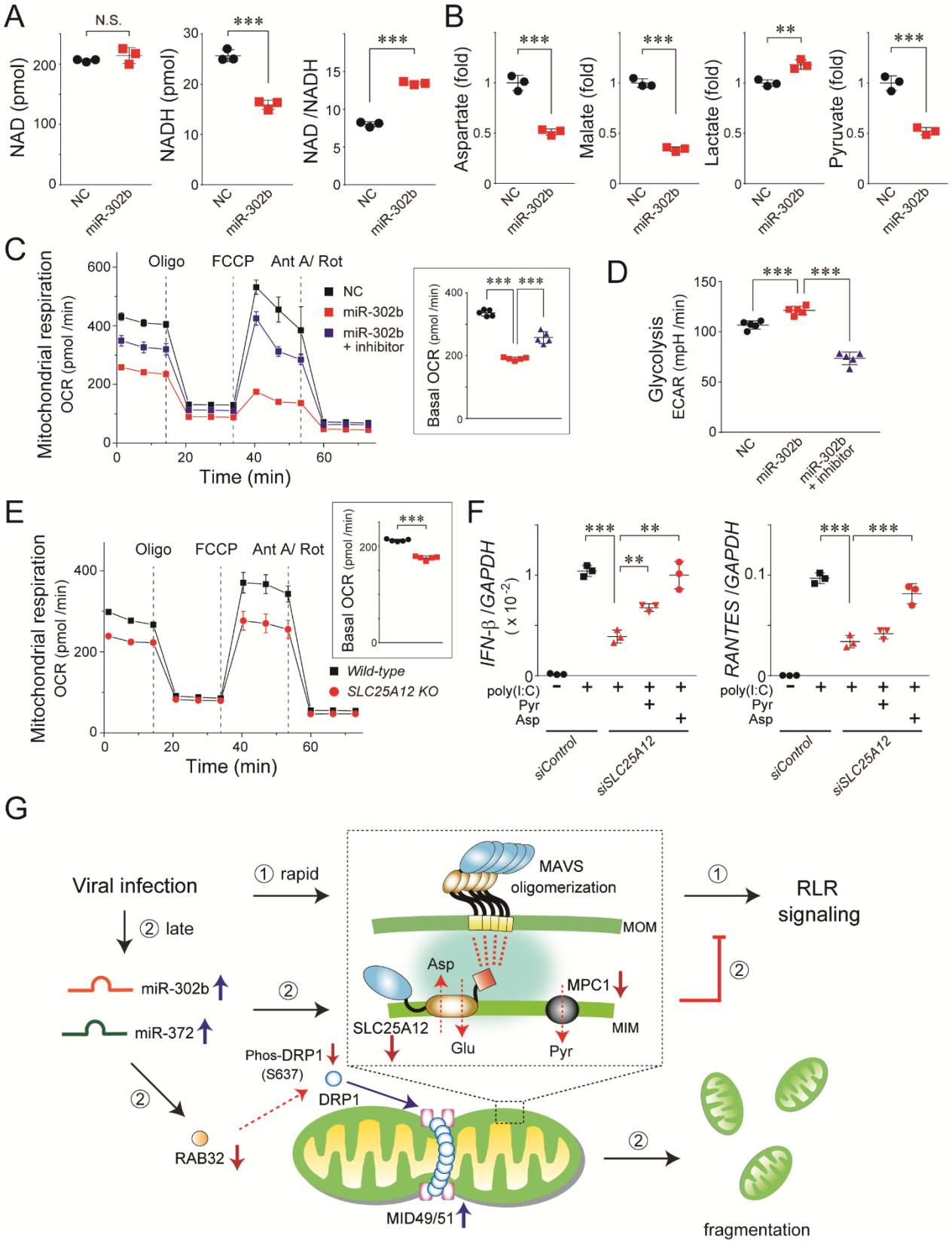
A
N.S.
***
***
NAD (pmol)
NADH (pmol)
NAD /NADH
NC
miR-302b
B
***
***
**
***
Aspartate (fold)
Malate (fold)
Lactate (fold)
Pyruvate (fold)
C
Oligo
FCCP
Ant A/ Rot
Mitochondrial respiration
OCR (pmol /min)
Time (min)
NC
miR-302b
miR-302b
+ inhibitor
Basal OCR (pmol /min)
D
Glycolysis
ECAR (mpH /min)
miR-302b
+ inhibitor
E
Wild-type
SLC25A12 KO
F
IFN-β /GAPDH
(x 10-2)
RANTES /GAPDH
poly(I:C)
Pyr
Asp
siControl
siSLC25A12
G
Viral infection
① rapid
② late
miR-302b
miR-372
MAVS
oligomerization
MOM
MIM
Asp
Glu
Pyr
MPC1
SLC25A12
Phos-DRP1
(S637)
DRP1
RAB32
MID49/51
RLR
signaling
fragmentation

Figure 10

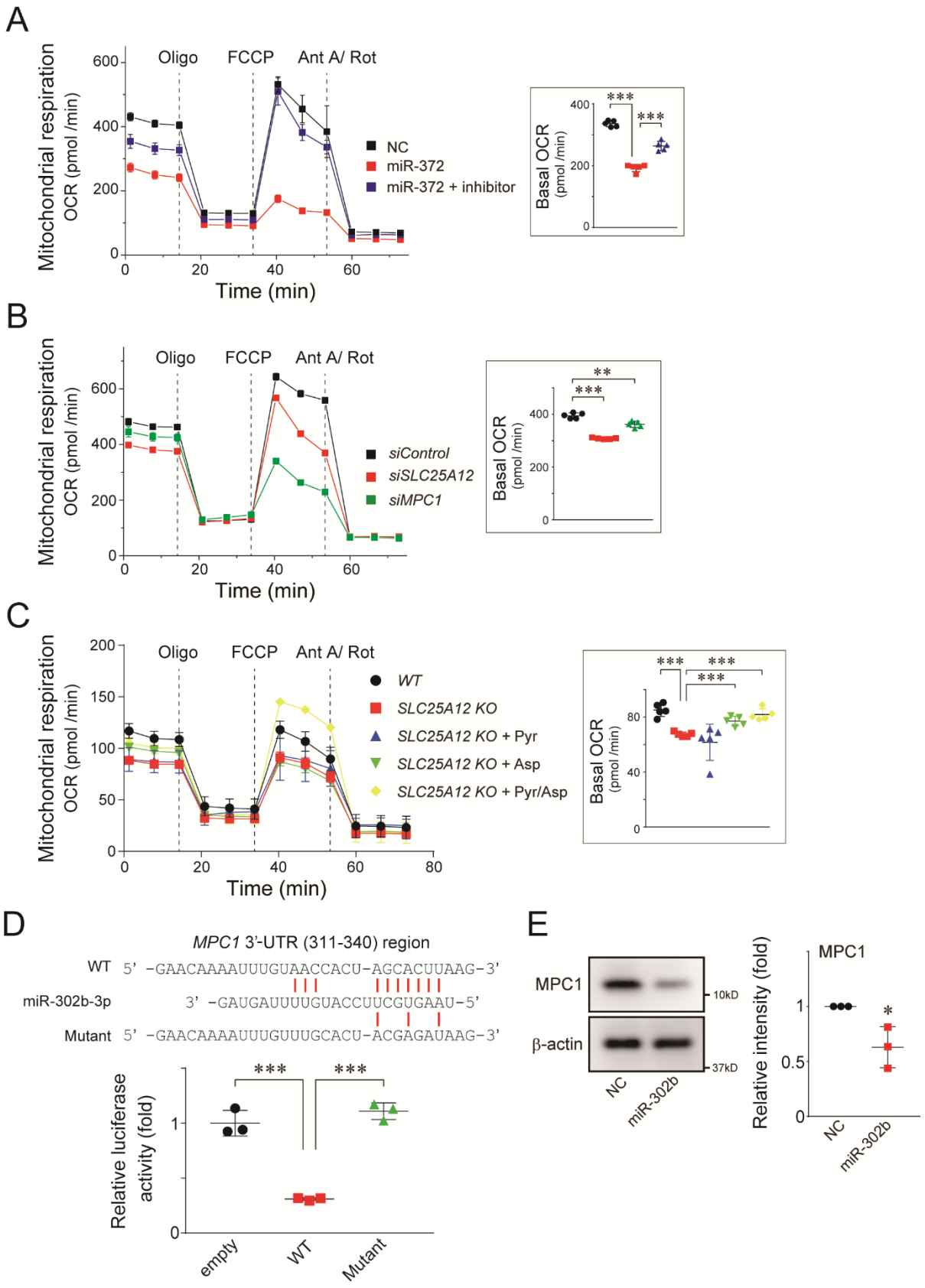
A
Mitochondrial respiration
OCR (pmol /min)
Oligo
FCCP
Ant A/ Rot
Time (min)
NC
miR-372
miR-372 + inhibitor
Basal OCR
(pmol /min)
B
siControl
siSLC25A12
siMPC1
C
WT
SLC25A12 KO
SLC25A12 KO + Pyr
SLC25A12 KO + Asp
SLC25A12 KO + Pyr/Asp
D
MPC1 3'-UTR (311-340) region
WT 5' -GAACAAAAUUUGUAACCACU-AGCACUUAAG-3'
miR-302b-3p 3' -GAUGAUUUUGUACCUUCGUGAAU-5'
Mutant 5' -GAACAAAAUUUGUUUGCACU-ACGAGAUAAG-3'
Relative luciferase activity (fold)
empty
WT
Mutant
E
MPC1
β-actin
10kD
37kD
NC
miR-302b
Relative intensity (fold)

KEY RESOURCES TABLE

REAGENT or RESOURCE	SOURCE	IDENTIFIER
Antibodies		
Anti-MAVS polyclonal antibody	abcam	Cat#: ab31334
Anti-MAVS polyclonal antibody	Thermo Fisher Scientific	Cat#: PA5-17256
Anti-c-Myc antibody [9E10]	abcam	Cat#: ab32
Anti-c-Myc antibody [9E10]	Covance	Cat#: MMS-150P
Anti-SLC25A12 antibody [EPR16294]	abcam	Cat#: ab200201
Anti-IRF3 (phospho S386) antibody [EPR2346]	abcam	Cat#: ab76493
Anti-REA (PHB2) antibody [EPR14522]	abcam	Cat#: ab181838
mtHsp70/Mitochondrial Heat Shock Protein 70 Antibody (JG1)	Thermo Fisher Scientific	Cat#: MA3-028
Monoclonal Anti-HA antibody	Sigma-Aldrich	Cat#: H3663
Anti-Rab32	Sigma-Aldrich	Cat#: SAB4200086
IRF3 (D83B9) Rabbit mAb	Cell Signaling Technology	Cat#: 4302
DRP1 (D6C7) Rabbit mAb	Cell Signaling Technology	Cat#: 8570
MCP1 (D2L9I) Rabbit mAb	Cell Signaling Technology	Cat#: 14462
Phospho-DRP1 (Ser637) (D3A4) Rabbit mAb	Cell Signaling Technology	Cat#: 6319
VDAC (D73D12) Rabbit mAb	Cell Signaling Technology	Cat#: 8674
GAPDH (14C10) Rabbit mAb (Biotinylated)	Cell Signaling Technology	Cat#: 5014
PHB1 Antibody	Cell Signaling Technology	Cat#: 2426
SMCR7/MID49 Polyclonal antibody	Proteintech	Cat#: 16413-1-AP
SMCR7L/MID51 Polyclonal antibody	Proteintech	Cat#: 20164-1-AP
β-Actin (C4)	Santa Cruz	Cat#: sc-47778
Anti-rabbit IgG, HRP-linked Antibody	Cell Signaling Technology	Cat#: 7074
Anti-mouse IgG, HRP-linked Antibody	Cell Signaling Technology	Cat#: 7076
Goat anti-Mouse IgG (H+L) Highly Cross-Adsorbed Secondary Antibody, Alexa Fluor 568	Thermo Fisher Scientific	Cat#: A11031
Chemicals and Reagent		
L-Glutamine	Thermo Fisher Scientific	Cat#: 25030
Sodium Pyruvate	Thermo Fisher Scientific	Cat#: 11360
Forskolin	Sigma-Aldrich	Cat#: F3917
FuGENE HD Transfection Reagent	Promega	Cat#: E2311
Lipofectamine 2000 Transfection Reagent	Thermo Fisher Scientific	Cat#: 11668

Lipofectamine RNAiMAX Transfection Reagent	Thermo Fisher Scientific	Cat#: 13778
Complete, Mini, EDTA-free	Roche Applied Science	Cat#: 1836170
Pierce IP Lysis Buffer	Thermo Fisher Scientific	Cat#: 87787
Fetal Bovine Serum, Dialyzed	Thermo Fisher Scientific	Cat#: 26400036
Poly(I:C)-LMW	Invivogen	Cat#: tlrl-picw
4%-Paraformaldehyde Phosphate Buffer Solution	Nacalai tesque	Cat#: 09154-14
Triton X-100	Nacalai tesque	Cat#: 35501-15
chloroform	Kanto Kagaku	Cat#: 07278-00
HEPES (1 M)	Thermo Fisher Scientific	Cat#: 15630
Sucrose	Wako	Cat#: 198-13525
D(+)-Glucose	Sigma-Aldrich	Cat#: 07-0680-5
D(-)-Mannitol	Nacalai tesque	Cat#: 11662-42
Sample Buffer Solution with Reducing Reagent(6x) for SDS-PAGE	Nacalai tesque	Cat#: 09499-14
Critical Commercial Assays		
Dual-Glo Luciferase Assay Symtem	Promega	Cat#: E2920
Steady-Glo Luciferase Assay System	Promega	Cat#: E2510
NanoBRET Nano-Glo Substrate	Promega	Cat#: N1571
Human interferon-β ELISA kit	Kamakura Techno-Science	Cat#: KTS301
Human IFN-β Quantikine ELISA Kit	R&D Systems	Cat#: DIFNB0
Seahorse XF Cell Mito Stress Test Kit	Agilent Technologies	Cat#: 103015-100
QuantiTect Reverse Transcription Kit	Qiagen	Cat#: 205313
TaqMan MicroRNA Reverse Transcription Kit	Thermo Fisher Scientific	Cat#: 4366596
TaqMan Fast Advanced Master Mix	Applied Biosystems	Cat#: 4444557
SuperSignal West Femto Maximum Sensitivity Substrate	Thermo Fisher Scientific	Cat#: 1859022
miRNeasy Mini Kit	Qiagen	Cat#: 217004
Maxwell 16 LEV simplyRNA Cells Kit	Promega	Cat#: AS1270
TaqMan Array Human MicroRNA A+B Cards Set v3.0	Applied Biosystems	Cat#: 4444913
TaqMan Gene Expression Assays		
GAPDH	Applied Biosystems	Assay ID: Hs02786624_g1
IFNB1	Applied Biosystems	Assay ID: Hs01077958_s1
CCL5	Applied Biosystems	Assay ID: Hs00982282_m1
TNF	Applied Biosystems	Assay ID: Hs00174128_m1
MPC1	Applied Biosystems	Assay ID: Hs00211484_m1

SLC25A12	Applied Biosystems	Assay ID: Hs00186535_m1
RAB32	Applied Biosystems	Assay ID: Hs00199149_m1
MIEF1 (MID51)	Applied Biosystems	Assay ID: Hs01007730_g1
MIEF2 (MID49)	Applied Biosystems	Assay ID: Hs02572417_s1
MFN1	Applied Biosystems	Assay ID: Hs00966851_m1
MFN2	Applied Biosystems	Assay ID: Hs00208382_m1
OPA1	Applied Biosystems	Assay ID: Hs01047013_m1
FIS1	Applied Biosystems	Assay ID: Hs00211420_m1
MFF	Applied Biosystems	Assay ID: Hs00697394_g1
DNM1L	Applied Biosystems	Assay ID: Hs01552605_m1
MAVS	Applied Biosystems	Assay ID: Hs00920075_m1
TaqMan MicroRNA Assays		
hsa-miR-302b	Applied Biosystems	Assay ID: 000531
hsa-miR-372	Applied Biosystems	Assay ID: 000560
U6 snRNA	Applied Biosystems	Assay ID: 001973
miRNA mimic		
mirVana miRNA mimic, has-miR-302b-3p	Thermo Fisher Scientific	Assay ID: MC10081
mirVana miRNA mimic, hsa-miR-372-3p	Thermo Fisher Scientific	Assay ID: MC10165
mirVana miRNA mimic, Negative Control #1	Thermo Fisher Scientific	Cat#: 4464058
miRNA inhibitor		
mirVana miRNA inhibitor, has-miR-302b-3p	Thermo Fisher Scientific	Assay ID: MH10081
mirVana miRNA inhibitor, hsa-miR-372-3p	Thermo Fisher Scientific	Assay ID: MH10165
mirVana miRNA inhibitor, Negative Control #1	Thermo Fisher Scientific	Cat#: 4464076
siRNA		
GeneSolution siRNA, Hs_RAB32_3: TGGGTTACAGATGTCATGTTA	Qiagen	Cat#: SI00092246
GeneSolution siRNA, Hs_SLC25A12_1: ATGGAGCTTGTTCGTAAGATA	Qiagen	Cat#: SI00054929
GeneSolution siRNA, Hs_BRP44L_5: AGCTGAGAGTTTCTAAACCAA	Qiagen	Cat#: SI04153415
siDrp1: AAGCAGAAGAATGGGGTAAAT	Qiagen	Custom oligo
AllStars Negative Control siRNA	Qiagen	Cat#: 1027280
Other		

DMEM, high glucose	Thermo Fisher Sceintific	Cat#: 11965
IMDM, GlutaMAX Supplement	Thermo Fisher Sceintific	Cat#: 31980
DMEM, no glucose, no phenol red, no glutamine	Thermo Fisher Sceintific	Cat#: A14430
XF Base Medium	Agilent Technologies	Cat#: 102353-100
Opti-MEM I Reduced Serum Medium, no phenol red	Thermo Fisher Scientific	Cat#: 11058
Cell Lines		
HEK293	ECACC	EC85120602
HeLa	ATCC	CCL-2
A549	ATCC	CCL-185
MRC-5	ATCC	CCL-171
HAP1 SLC25A12 knockout (2bp deletion in exon 8)	Horizon	HZGHC001735c010
HAP1 (parental)	Horizon	C631